Draft version August 25, 2026
Typeset using LaTeX **twocolumn** style in AASTeX631

arXiv:2608.23534v1 [astro-ph.IM] 24 Aug 2026

Strong Lensing Cosmology with Population-level Calibrated Neural Ratio Estimation

Sreevani Jarugula [1], Brian D. Nord [1,2,3,*], Aleksandra Ćiprijanović [1,2,4] and Shubhendu Trivedi [1,†]

[1] *Scientific Computing Division, Fermi National Accelerator Laboratory, Batavia, IL 60510*
[2] *Department of Astronomy and Astrophysics, University of Chicago, Chicago, IL 60637*
[3] *KICP, University of Chicago, Chicago, IL 60637*
[4] *NSF-Simons AI Institute for the Sky (SkAI), 172 E. Chestnut St., Chicago, IL 60611*

ABSTRACT

Strong gravitational lensing contains key information about cosmic acceleration. Modern and next-generation galaxy imaging surveys are expected to provide high-quality data on $\mathcal{O}(10^5)$ galaxy-galaxy lensing systems. The plethora and complexity of the data are likely to present computational challenges for parameter inference methods for fitting high-dimensional likelihoods, which are often analytically intractable. Neural Ratio Estimation (NRE) efficiently computes individual likelihood ratios that can be combined into population-level posteriors. We use simulations to study the capacity of NRE to jointly predict the dark energy equation-of-state parameter w and the total matter density Ω_m from lensing images and companion spectroscopic information. We also introduce a post hoc posterior coverage calibration procedure that mitigates the model overconfidence that is typically found in neural density estimation applications. Our experiments show that the errors on both parameters decrease with increasing inference population sizes. In particular, for 100 lenses in a standard ΛCDM Universe, our calibrated NRE model achieves median fractional uncertainty of 22.8% in w and 2.9% in Ω_m. This proof of concept demonstrates a potentially scalable approach for efficient cosmological parameter inference with large populations of galaxy-scale lenses observed in future surveys.

1. INTRODUCTION

In the standard cosmological model (ΛCDM), the evolution of a flat Universe is driven by two major components. First, the total matter density Ω_m, mostly comprising Dark Matter (DM), which drives the hierarchically forming and gravitationally bound large-scale structures – from subhaloes to galaxies to the cosmic web. Second, space-time is accelerating in its expansion due to Dark Energy (DE), which is a scalar field characterized by an equation of state with pressure-density ratio $w = p/\rho$. In a Universe with a flat geometry the DE density is determined exactly by the total matter density, where $\Omega_{\rm DE} = 1 - \Omega_m$ and in ΛCDM, the equation of state is fixed at $w = -1$. The fundamental natures of both DE and DM remain unknown, and modern experiments use combinations of complementary probes – e.g., the Cosmic Microwave Background (CMB), the cosmic distance ladder, galaxy clusters and clustering, and gravitational lensing – to constrain cosmological parameters.

Many combinations of probes have found consistency with the ΛCDM (Planck Collaboration 2020). However, investigations of systematics effects and updated joint probe analyses have uncovered significant disagreement in cosmology parameters (Leizerovich et al. 2023). In particular, the Hubble Tension originates in estimates of H_0 that are $> 4\sigma$ higher from the cosmic distance ladder than from the CMB measurements (Freedman 2021; Riess et al. 2022; Feeney et al. 2018; Di Valentino et al. 2021; Huterer 2023; Khalife et al. 2024; Cai & Wang 2026). Secondarily, the S_8 Tension arises from estimates of $S_8 \equiv \sqrt{\Omega_m/0.3}\sigma_8$ that are $\sim 3\sigma$ lower from galaxy surveys than from CMB experiments (Poulin et al. 2023; Joseph et al. 2023; Pantos & Perivolaropoulos 2026). These discrepancies may indicate new physics in the form of systematic effects in individual probes or an updated cosmological model (e.g., McCarthy et al. 2023; Kamionkowski & Riess 2023; Zu et al. 2026). These discrepancies invite the collection of larger, more information-dense data sets and the development of analysis techniques that maximize the extraction of information from existing and new cosmological probes.

Complementary to other probes, strong gravitational lensing can constrain DE, DM, and the expansion rate through distances and the large-scale structure. Dif-

* Now Independent Researcher
† Now at Google DeepMind

ferent lens configurations provide access to different parameters. Time-delay cosmography (Refsdal 1964) relies on quasars or supernovae to constrain the Hubble constant and is independent of all the other probes (Tortora et al. 2004; Ding et al. 2021; Sonnenfeld 2021; Treu et al. 2022; Treu & Shajib 2024; Li et al. 2024). There exist dedicated long-term programs like H0LiCOW to make high-precision measurements of H_0 (Suyu et al. 2017), which have led to corroborating evidence of the Hubble Tension (Wong et al. 2020). Alternatively, through the ratio of angular diameter distances, static galaxy-galaxy lensing provides H_0-independent joint constraints on w and Ω_m when the lens stellar velocity dispersion is known (Futamase & Yoshida 2001; Koopmans 2006; Li & Chen 2023). State-of-the-art image-based model-fitting of individual lenses relies on Monte Carlo sampling of analytic, tractable (i.e., Gaussian) likelihoods to produce posteriors. After deriving lens parameters, further population-level analytic modeling of $\mathcal{O}(10) - \mathcal{O}(10^2)$ lenses gives constraints on w-Ω_m (Chen et al. 2019; Cao et al. 2015; Biesiada et al. 2010; Li et al. 2024), but still requiring assumptions of tractable Gaussian parameter distributions.

Several modern experiments — the Vera Rubin Observatory's Legacy Survey of Space and Time (LSST; Ivezic et al. 2008; Shajib et al. 2025), the Euclid Wide Survey (Euclid Collaboration 2022; Lines et al. 2025), the Roman Space Telescope High Latitude Wide Area Survey (Spergel et al. 2015), and the China Space Station telescope (CSST; Cao et al. 2024) — are expected to obtain data on $\mathcal{O}(10^5)$ strong lenses (Holloway et al. 2023). Spectroscopic projects, such as the 4MOST Strong Lensing Spectroscopic Legacy Survey (4SLSLS; Collett et al. 2023) and the Dark Energy Spectroscopic Instrument (DESI; Avirett-Mackenzie & Tojeiro 2021; Ferrami & Wyithe 2025), can supply redshift and velocity-dispersion measurements needed for lens models to constrain w and Ω_m. Nevertheless, modeling galaxy-scale lenses is highly computationally expensive. Therefore, more efficient lens modeling techniques and more flexible parameter inference approaches may be necessary to exhaust the capacity of very large next-generation data sets.

Artificial Intelligence (AI) models are characterized by their numerous internal parameters, which makes them be useful for predictions from large and complex data sets. In particular, Simulation-based Inference (SBI) is a growing suite of AI-based methods for parameter inference when high-fidelity data simulators are available and likelihoods are high-dimensional and intractable (Cranmer et al. 2020; Tejero-Cantero et al. 2020; Zeghal et al. 2022; Gloeckler et al. 2024; Deistler et al. 2025; Franco Abellán et al. 2025). When output densities must be expressive (i.e., non-Gaussian), Neural Likelihood Estimation (NLE; Papamakarios et al. 2019; Bastide et al. 2025; Emma & Ashton 2026), Neural Posterior Estimation (NPE; Papamakarios & Murray 2016; Greenberg et al. 2019), Neural Score Estimation (Sharrock et al. 2022; Remy et al. 2023; Barco et al. 2025), Surjective Sequential Neural Likelihood (SSNL Dirmeier et al. 2023) employ flexible density estimators, like normalizing and masked autoregressive flows (Kingma et al. 2016; Papamakarios et al. 2019, 2017) and diffusion (Linhart et al. 2024; Rosso & Mayo 2025). NPE has been used to estimate parameters of individual objects across numerous phenomena in astrophysics and cosmology, especially for gravitational wave (GW) signals (Green et al. 2020; Dax et al. 2021; Kolmus et al. 2024) and strong lens images (Legin et al. 2021, 2023; Swierc et al. 2024; Poh et al. 2025; Dhanasingham et al. 2025; Erickson et al. 2025).

However, estimating cosmological parameters shared by an entire population is the goal under consideration. In general, it is not formally permissible to combine posteriors from individual objects into a single global posterior, so conventional NPE is not appropriate. Hierarchical Neural Posterior Estimation (HNPE) and related methods have been developed, but not widely tested (Rodrigues et al. 2021; Fan & White 2025; Tran et al. 2017). Additionally, a novel approach in GW astronomy learns the population posterior from individually learned sub-population posteriors (Leyde et al. 2024). Combining NLE outputs for population-level parameter estimates does not appear to have been implemented in the literature. Alternatively, Neural likelihood Ratio Estimation (NRE; Brehmer et al. 2020; Hermans et al. 2020; Miller et al. 2021) uses relatively simple classification neural networks instead of flows or diffusion models and has been expanded and refined through multiple studies in physics and astronomy (Cole et al. 2022; Zhang et al. 2022; Miller et al. 2022; Cobb et al. 2023; Anau Montel et al. 2024; Rizvi et al. 2024). Ratios from individual lenses can be combined and then joined with a prior to achieve posteriors of lens population distributions (Brehmer et al. 2019).

Inferences require strict assessment for fidelity and trustworthiness. In this regard, SBI has been the subject of intensive study and the target of new diagnostics and metrics. Simulation-based calibration (SBC) describes a growing suite of diagnostics of posterior quality (Talts et al. 2018; Lueckmann et al. 2021) – e.g., rank statistic histograms, posterior coverage, and TARP (Lemos et al. 2023). Many studies show that SBI models tend to be overconfident, generating posteriors that are too

narrow (Hermans et al. 2021). Balanced NRE (BNRE) is designed to mitigate overconfidence by increasing uncertainties in parameter regimes (Delaunoy et al. 2022); BNRE has not yet been applied explicitly in population-level inference. Post hoc calibration of ratios with histograms aims to correct inferences (Brehmer et al. 2019), but statistical guarantees haven't been demonstrated explicitly. Frazier et al. (2024) show that neural estimators can, in principle, match the statistical guarantees of established methods such as approximate Bayesian computation, but only for well-specified models. In practice, however, no density estimator or post hoc calibration method yet guarantees a correctly calibrated posterior for real data. The tendency toward overconfidence therefore remains the central obstacle to trustworthy SBI.

In this work, we study the capacity of NRE for deriving trustworthy constraints on w and Ω_m from populations of galaxy-galaxy lenses. We present a proof of concept that focuses on 1) building a population-level posterior from individual likelihood ratios and 2) mitigating the longstanding tendency of SBI models to be overconfident. Therefore, we reduce the computational burden – i.e., allow for a simpler classification network – by assuming an idealized context for the data. The NRE model uses two inputs: the input simulated lens images with simplified lens models and a single band and spectroscopically derived parameters. After combining the likelihood ratios of individual lenses, we apply a novel post hoc calibration method to mitigate posterior overconfidence. Finally, we analyze the confidence and accuracy of the model with and without calibration.

In Sec. 2, we introduce strong gravitational lensing theory, including the degeneracy between the two cosmological parameters of interest. Then, in Sec. 3, we describe our study's data sets for model-building and testing — all of which are derived from simulations. Sec. 4 contains a brief derivation of the NRE approach for population-level posterior estimation, the NRE model architecture and training; it also introduces our post hoc calibration procedure. Sec. 5 describes the main results of the experiments. In Sec. 6, we discuss the stress tests and current limitations of the NRE-based approach presented here. In Sec. 7, we recapitulate the key findings of this study, accompanied by an outlook on potential future analyses. Finally, in the Appendix, we provide additional details on the NRE model architecture and stress tests of the model.

2. STRONG GRAVITATIONAL LENSING

Strong gravitational lensing occurs when a massive object, such as a galaxy (lens), deflects the light from a background object (source) to produce magnified and distorted images of the source in the image plane. For a point-like source, such as a QSO or a supernova, lensing can create multiple images of the source. The basic formalism below introduces galaxy-galaxy lensing, where the source is a galaxy (an extended object), and lensing causes arc-like structures in the image plane. More detailed discussions can be found in Treu (2010); Saha et al. (2024); Shajib et al. (2024).

2.1. *Formalism*

The lens equation relates the source position β to the lensed source position θ through the deflection angle $\alpha(\theta)$ as

$$\beta \ = \theta \ - \alpha(\theta). \tag{1}$$

The deflection field is the gradient of the lensing potential ψ:

$$\alpha(\theta) \ = \nabla\psi(\theta) \ = \frac{1}{\pi}\int d\theta' \ \frac{\theta \ - \theta'}{|\theta \ - \theta'|^2}\kappa(\theta'), \tag{2}$$

where the convergence $\kappa(\theta) = \Sigma(\theta)/\Sigma_{cr}$, and $\Sigma(\theta)$ is the deflector mass surface density projected onto the lens plane. The critical mass surface density Σ_{cr} is

$$\Sigma_{cr} \ = \frac{1}{4\pi \ G}\frac{D_\mathrm{s}}{D_\mathrm{ls}D_\mathrm{l}}, \tag{3}$$

where G is the gravitational constant; and D_l, D_s, and D_ls are the angular diameter distances between the observer and the lens, the observer and the source, and the lens and the source, respectively. In wCDM cosmology (where w can vary from -1), D depends on the the source and lens redshifts (z_s and z_l, respectively) and on the cosmological parameters (H_0, Ω_m, and w):

$$D(z, H_0, \Omega_m, w) \ = \frac{1}{1+z}\frac{c}{H_0}\int_0^z \frac{dz'}{h(z', \Omega_m, w)}, \tag{4}$$

where the Hubble parameter is

$$h^2(z, \Omega_m, w) \ = \Omega_m(1+z)^3 + (1-\Omega_m)(1+z)^{3(1+w)}. \tag{5}$$

For a circular deflector (i.e., lens), the Einstein radius θ_E is the radius within which the average surface mass density is equal to the critical density so that the average convergence $\langle\kappa\rangle = 1$.

In the case of non-circular deflectors, the mass enclosed within the Einstein radius is (Kormann et al. 1994)

$$\theta_\mathrm{E} \ = \sqrt{\frac{4GM(\theta_\mathrm{E})}{c^2}\frac{D_\mathrm{ls}}{D_\mathrm{l}D_\mathrm{s}}}. \tag{6}$$

The majority of the lenses are early type (elliptical) galaxies, whose mass densities are well described by an

SIE profile (Oguri & Marshall 2010), where the Einstein radius becomes

$$\theta_{\rm E} = 4\pi \left(\frac{\sigma_{\rm v}}{c}\right)^2 \frac{D_{\rm ls}}{D_{\rm s}}, \quad (7)$$

where $\sigma_{\rm v}$ is the stellar velocity dispersion, and c is the speed of light (Kormann et al. 1994). The convergence of a lens with an SIE profile is

$$\kappa(x_{\phi_{\rm l}}, y_{\phi_{\rm l}}) = \frac{1}{2}\left(\frac{\theta_{\rm E}}{\sqrt{q_{\rm l} x_{\phi_{\rm l}}^2 + y_{\phi_{\rm l}}^2/q_{\rm l}}}\right), \quad (8)$$

where $(x_{\phi_{\rm l}}, y_{\phi_{\rm l}})$ are the positions aligned to the major and minor lens axes, $q_{\rm l}$ is the major/minor axis ratio, and $\phi_{\rm l}$ is the angle of rotation between $(x_{\phi_{\rm l}}, y_{\phi_{\rm l}})$ and the centre of the lens mass coordinates $(x_{\rm l},\ y_{\rm l})$ in the image plane. The lens ellipticity is related to the major and minor axis as

$$\begin{aligned} l_{\rm e1} &= \frac{1-q_{\rm l}}{1+q_{\rm l}} cos(2\phi_{\rm l}), \\ l_{\rm e2} &= \frac{1-q_{\rm l}}{1+q_{\rm l}} sin(2\phi_{\rm l}). \end{aligned} \quad (9)$$

We do not include external shear in our analysis.

We model the source light distribution with a Sérsic profile (Sersic 1968):

$$I(r) = I_e exp\left(-b_n\left(\left(\frac{r}{R}\right)^{1/n} - 1\right)\right), \quad (10)$$

where I_e is the intensity at the effective radius R, and $r = \sqrt{q_{\rm s} x_{\phi_{\rm s}} + y_{\phi_{\rm s}}/q_{\rm s}}$; the positions $(x_{\phi_{\rm s}}, y_{\phi_{\rm s}})$ are aligned to the semimajor axis of the Sérsic light profile, and $q_{\rm s}$ is the source major-to-minor axis ratio. In the range $0 < n < 10$, the coefficient b can be approximated as (Ciotti & Bertin 1999)

$$b_n \approx 2n - \frac{1}{3} + \frac{4}{405n} + \frac{46}{25515n^n}. \quad (11)$$

Finally the source ellipticity is

$$\begin{aligned} s_{\rm e1} &= \frac{1-q_{\rm s}}{1+q_{\rm s}} cos(2\phi_{\rm s}), \\ s_{\rm e2} &= \frac{1-q_{\rm s}}{1+q_{\rm s}} sin(2\phi_{\rm s}). \end{aligned} \quad (12)$$

2.2. *Degeneracy in cosmology parameters*

For SIE lenses in a flat wCDM cosmology, the Einstein radius is fully specified by the velocity dispersion, the lens and source redshifts, and the cosmological parameters (see Eqn.'s 4 and 7). Even when the velocity dispersion and redshifts are known, varying combinations of w and Ω_m give the same Einstein radius: the cosmological parameters are degenerate with respect to a single lens. Therefore, an individual lens is insufficient to jointly infer w and Ω_m. However, two or more lenses, with different redshifts can increase the leverage for constraining capability of lens images.

We illustrate this behavior in Fig. 1, where two sets of contours show constant values of the Einstein radius with lens redshifts $z_{\rm l} = 0.1$ and $z_{\rm l} = 0.8$, respectively. Both configurations have the same source redshift $z_{\rm s} = 2.0$ and lens velocity dispersion $\sigma_{\rm v} = 275\,{\rm km\,s^{-1}}$. The true cosmology is indicated by a star. The curve for the Einstein radius for the single lens at redshift $z_{\rm l} = 0.1$ intersects the true cosmology, but does not constrain it. The curve for the radius at the other redshift $z_{\rm l} = 0.8$ intersects the low-redshift lens curve and the true cosmology, breaking the w-Ω_m degeneracy. In practice, modeling lens images adds uncertainty to the Einstein radius estimates, which would add a finite width to each contour curve. Two lenses constrain w and Ω_m only to the region where their broadened bands overlap, and adding more lenses progressively shrinks this region, tightening the constraints and averaging down the measurement scatter.

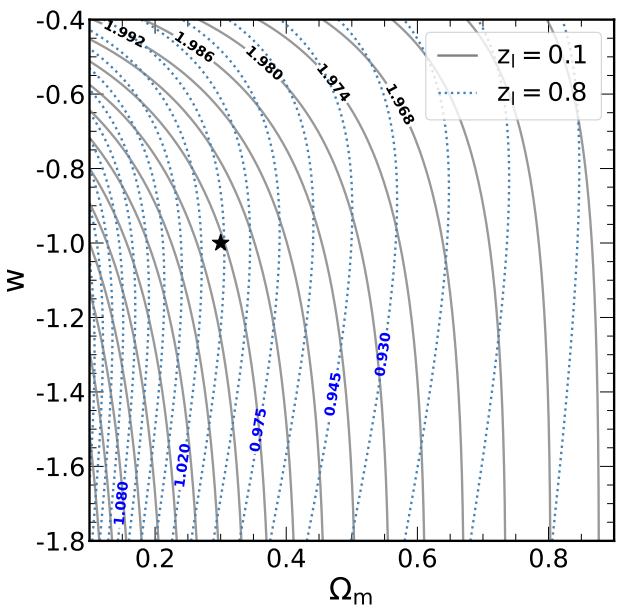

Figure 1. Einstein radius $\theta_{\rm E}$ (arcsec; Eqn. 7) as a function of w and Ω_m for lenses at low redshift ($z_{\rm l} = 0.1$; gray) and high redshift ($z_{\rm l} = 0.8$; blue). The configurations use the same source redshift ($z_{\rm s} = 2.0$) and stellar velocity dispersion ($\sigma_{\rm v}$=275 kms^{-1}). The canonical ΛCDM cosmology is marked with a star.

3. DATA

The lens model in this study uses the following parameters to produce lens images:

- cosmology parameters: w, Ω_m;
- lens and source redshift: $z_\mathrm{l}, z_\mathrm{s}$;
- lens stellar velocity dispersion: σ_v;
- lens mass profile: $x_\mathrm{l}, y_\mathrm{l}, l_\mathrm{e1}, l_\mathrm{e2}$;
- source light profile: $m_\mathrm{s}, R, n, s_\mathrm{e1}, s_\mathrm{e2}$.

The apparent magnitude m_s is typically obtained from observations so that it is used in place of the intensity I_e (Eqn. 10). We summarize some astrophysics parameters as $\zeta \equiv (z_\mathrm{l}, z_\mathrm{s}, \sigma_\mathrm{v})$, while the remaining nuisance astrophysics parameters are summarized with ν.

For w, we use a uniform prior $\mathcal{U}(-1.8, -0.35)$. The upper bound is motivated by the physical requirement $w < -1/3$, while the lower bound is chosen to provide a generous margin around the current observational consensus of $w = -1$. For Ω_m, we assume a uniform prior $\mathcal{U}(0.1, 0.9)$. This range ensures the total matter density remains strictly positive and well-defined, while allowing the model to include a wide range of cosmologies near 0.3, which is favored by current observations. We fix $H_0 = 70\,\mathrm{km\,s^{-1}\,Mpc^{-1}}$.

The lens position $(x_\mathrm{l}, y_\mathrm{l})$ is drawn from a normal distribution centered at zero because the lens is assumed to be near the center of the image. The source position is fixed at the image center (0,0). The priors for ζ encompass the peak of the parameter distributions from the realistic DES lens simulations (Collett 2015). These parameters typically have significant observational errors; however, to keep the model training simple, ζ are used as exact inputs for the model. All the other parameters have uniform priors that bound current observations. The astrophysical parameters are sampled independently of the cosmological parameters and independently of each other. The prior ranges in the training data are listed in Table 1.

To produce images representative of survey observing conditions, we adopt instrumental and observational characteristics from DES Data Release 1 (DES Collaboration 2018). We use a pixel scale of 0.263 arcsec pixel^{-1}, a CCD gain of 6.083 e^-/count, and a read noise of 7.0 e^-. We select the g-band filter to maximize contrast for the lensing arcs in the images: lens galaxies are typically red ellipticals that are fainter at bluer wavelengths, and source galaxies are often bluer, star-forming galaxies that are brighter in the g band. The sky brightness, seeing, and effective number of exposures are based on empirical survey values; the magnitude zero point is set to 30.0. We assume that the lens light is perfectly subtracted from the images. In practice, lens light subtraction is commonly performed prior to lens modeling, and some automated approaches have been tested (Hezaveh et al. 2017). All images have a size of 32×32 pixels. We simulate lens images with `deeplenstronomy` (Morgan et al. 2021), which is built on `lenstronomy` (Birrer et al. 2015; Birrer & Amara 2018).

We use four data sets to build the NRE model: training, validation, test, and calibration. The training and validation datasets consist of 1,990,000 and 398,000 images, respectively. We sample the cosmology and astrophysics parameters according to the priors in Table 1. Examples of training images are shown in Fig. 2.

We construct 10 independently sampled test datasets – the Entire Region and nine Sub-Regions within the Entire Region. The astrophysics parameter test priors are the same as those used for training. For the cosmology parameter priors, the test ranges are chosen to be well within the training ranges to prevent edge-effect biases in model prediction. The Entire Test Set encompasses nine smaller Sub-Regions. Within each test region (Entire Test Region or Sub-Region), we sample 100 pairs of cosmological parameters (w, Ω_m) according to the priors in Table 2 and Fig. 3 and for each cosmology pair, we generate 100 lenses according to the priors in Table 1.

For the calibration dataset, we sample 50 pairs of cosmological parameters and for each cosmology, we generate 100 lenses. Further details of the calibration dataset and procedure are provided in Sec. 4.3.

All images are preprocessed before being passed to the neural network. Each image is first normalized by dividing by the sum of its pixel values over the spatial dimensions, ensuring unit total intensity. The images are then multiplied by the total number of pixels, rescaling them such that the average pixel value is unity while preserving the relative spatial intensity distribution.

The training and test datasets are publicly available on Zenodo[1]. The code used in this analysis is available in our GitHub repository[2].

4. METHOD: POSTERIORS FROM NEURAL RATIO ESTIMATION

Our primary goal is population-level inference through the combination of multiple individual lens likelihoods in a population: therefore, NPE is not an option. We also seek the simplest model (i.e., the least amount of parameters and the simplest architecture): therefore, NLE is not the best option. NRE remains the best viable

[1] https://zenodo.org/records/20804324

[2] https://github.com/deepskies/CosmoLensNRE

Table 1. Prior parameter distributions for generating training and validation data.

Parameter	Name	Priors
	Cosmology	
w	Dark Energy equation of state	$\mathcal{U}(-1.8, -0.35)$
Ω_m	Total Matter density	$\mathcal{U}(0.1, 0.9)$
H_0 [km/s/Mpc]	Hubble constant	70.0
	Lens	
$\sigma_{\rm v}$ [km/s]	velocity dispersion	$\mathcal{U}(225, 300)$
$x_{\rm l}$ [arcsec]	lens position x	$\mathcal{N}(0.0, 0.8)$
$y_{\rm l}$ [arcsec]	lens position y	$\mathcal{N}(0.0, 0.8)$
$z_{\rm l}$	lens redshift	$\mathcal{U}(0.3, 0.8)$
$l_{\rm e1}$	lens ellipticity	$\mathcal{U}(-0.1, 0.1)$
$l_{\rm e2}$	lens ellipticity	$\mathcal{U}(-0.1, 0.1)$
	Source Light	
$m_{\rm s}$	magnitude	$\mathcal{U}(19, 24)$
R [arcsec]	half-light radius	$\mathcal{U}(0.1, 3.0)$
n	Sersic index	$\mathcal{U}(0.5, 8.0)$
$s_{\rm e1}$	source ellipticity	$\mathcal{U}(-0.1, 0.1)$
$s_{\rm e2}$	source ellipticity	$\mathcal{U}(-0.1, 0.1)$
$z_{\rm s}$	source redshift	$\mathcal{U}(1.5, 2.5)$

approach for this task. Next, we describe the theory and procedure for NRE in the context of cosmology, including population-level likelihood ratios and posterior sampling. We also present a novel post hoc calibration approach to mitigate model overconfidence.

4.1. *Population-level NRE for Cosmological Parameters*

By way of Bayes' Theorem, we write the posterior of the parameter η as

$$p(\eta|x) = \frac{p(x,\eta)}{p(x)} \tag{13}$$

$$= r(x \mid \eta)p(\eta), \tag{14}$$

where x is the data, $p(x,\eta)$ is the joint distribution, $p(x)$ is the evidence; and $r(x|\eta)$ is the likelihood-to-evidence ratio (LR) and is equivalent to the ratio between the joint distribution and the marginal distribution (Cranmer et al. 2015):

$$r(x|\eta) = \frac{p(x,\eta)}{p(x)p(\eta)}. \tag{15}$$

An optimal classifier may be written in terms of the joint distribution and the marginal distribution and therefore the LR:

$$d^*(x,\eta) = \frac{p(x,\eta)}{p(x,\eta) + p(x)p(\eta)} \tag{16}$$

$$= \frac{r(x|\eta)}{1 + r(x|\eta)}, \tag{17}$$

where joint distribution samples have class label $y = 1$ and marginal distribution samples have class label $y = 0$. Then, NRE may be constituted by writing the LR in terms of the optimal classifier (Hermans et al. 2020):

$$r(x|\eta) = \frac{d^*(x,\eta)}{1 - d^*(x,\eta)}. \tag{18}$$

In this study, the input data are the lens image x and the parameters ζ, w, Ω_m. The images are generated through the implicit likelihood of the parameters: $x \sim p(x|w, \Omega_m, \zeta, \nu)$ (see Sec. 3). Network training marginalizes over the nuisance parameters ν. Therefore, an NRE-derived LR for a single lensing object is

$$r(x, \zeta|w, \Omega_m) = \frac{d^*(x, \zeta, w, \Omega_m)}{1 - d^*(x, \zeta, w, \Omega_m)}, \tag{19}$$

where ζ is considered known (without uncertainty) for each lens, from other observations. The joint distribution $p(x, \zeta, w, \Omega_m)$ samples are labeled as class $y = 1$ and the marginal distribution $p(x, \zeta)p(w)p(\Omega_m)$ samples are labeled as class $y = 0$.

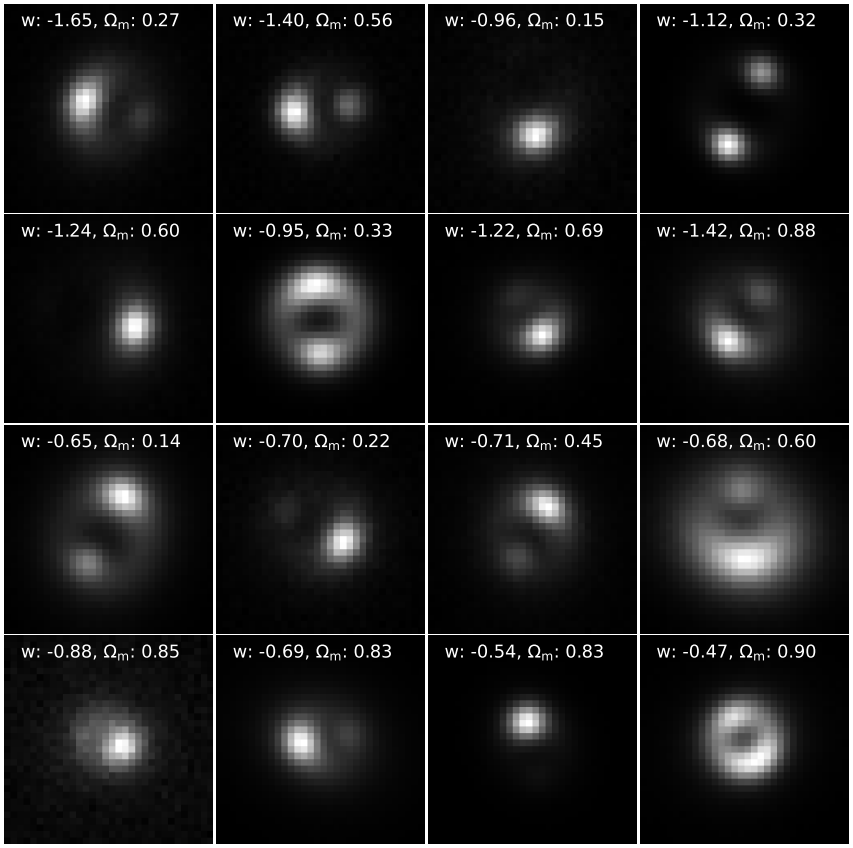

Figure 2. Randomly selected image examples from the training dataset. The images correspond to g-band observations with DES-like noise. Only the lensed source light is included, mimicking ideal lens-light subtraction.

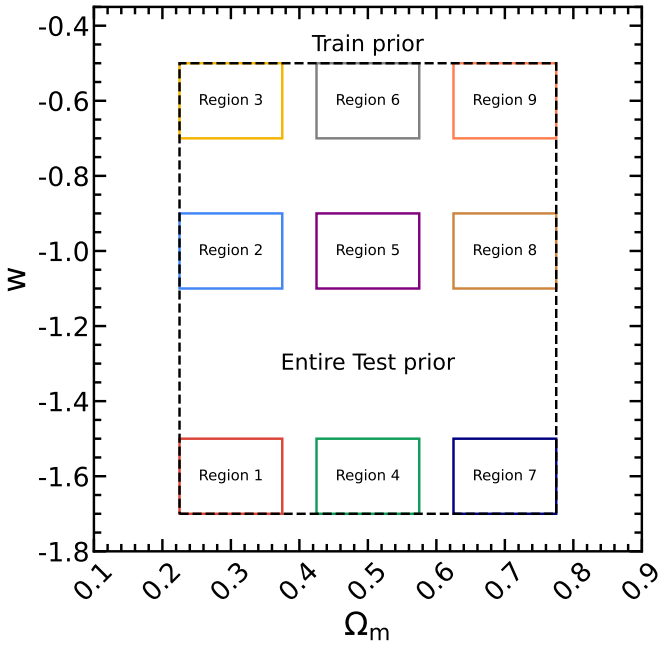

Figure 3. Priors used to generate the datasets in the w-Ω_m plane. The training prior comprises the full area displayed: $w \in [-1.8, -0.35]$ and $\Omega_m \in [0.1, 0.9]$. The priors for the Entire Test Region (dashed) and the nine Sub-Regions (colored boxes) are listed in Table 2.

The population-level LR for $\{x, \zeta\}$ can be obtained by combining the LR's from individual lenses under the assumption that the observations are i.i.d.:

$$\ln\ r(\{x,\zeta\}|w,\Omega_m) = \sum_i \ln\ r(x_i\zeta_i|w,\Omega_m). \qquad (20)$$

Finally, we use MCMC sampling to infer posteriors $p(w, \Omega_m|\{x, \zeta\})$ from the population-level log-LR. MCMC sampling with the Metropolis-Hastings algorithm (Hastings 1970) was implemented with `emcee` (Foreman-Mackey et al. 2013). We initiate five walkers randomly around a starting value of $w = -1.5$ and $\Omega_m = 0.31$. We implement a warm-up period with 200 steps, where the walkers converge to the target distribution. The position of the walkers is reset to the value that was converged on after each warm-up. After the warm-up, we run the sampling for 1000 steps. The prior range for w and Ω_m values is the same as the training prior. These raw posteriors are not yet calibrated to account for the expected model overconfidence.

4.2. *Simulation-based calibration*

Simulation-based Calibration (SBC; Talts et al. 2018) methods are used to diagnose calibration performance. A well-calibrated posterior distribution covers the true value $x\%$ of the time within $x\%$ of its posterior probability volume. Additionally, the rank statistic of the prior sample relative to well-calibrated posterior samples is uniformly distributed. However, when the rank histogram is $\cup$-shaped, the model posterior is narrower than the true posterior and underestimates the uncertainty, indicating an over-confident model. Alternatively, when the histogram is $\cap$-shaped, the model posterior is broader than the true posterior, indicating an under-confident model.

SBI models are generally susceptible to overconfidence, where the neural network produces a posterior distribution that is artificially narrow and can exclude the true physical parameters. This can lead to catastrophic model misspecification, which itself can lead to false rejection of theoretical models or the misinterpretation of systematic errors as new physics (Hermans et al. 2021). We use SBC to diagnose our models and to design a method for post hoc posterior calibration, which aims to mitigate SBI model overconfidence.

4.3. *Post hoc calibration*

Algorithms like Balanced Neural Ratio Estimation (BNRE), which enforces a balancing condition on the binary neural classifier, have been shown to yield more conservative and reliable posteriors (Delaunoy et al. 2022). There is also empirical evidence that an ensemble of models can produce more reliable posterior approximations (Hermans et al. 2021). In our preliminary experiments, we encountered model overconfidence that could not be addressed with increased training set sizes, longer training runs, or more refined input image data. In our attempts to use BNRE, the hyperparemter used to enforce the balance required arbitrary and non-data-driven choices – and remained insufficient for addressing model overconfidence. We didn't attempt ensemble modeling because it would be too computationally intensive.

Therefore, to address model overconfidence, we applied a post hoc calibration that aims to broaden posteriors across the w-Ω_m plane. We define the calibrated LR for a population of N lenses as a linearly scaled joint likelihood ratio:

$$\ln \hat{r}(\{x, \zeta\}|w, \Omega_m) = \Gamma \sum_{i=1}^{N} \ln r(x_i, \zeta_i|w, \Omega_m) + \Delta, \quad (21)$$

where Γ acts as a temperature-like scaling factor that adjusts the width (sharpness) of the posterior, and Δ is a global normalization offset that corrects for systematic biases in the population.

The optimal Γ and Δ values will yield a rank histogram close to a uniform distribution. Scalar metrics like χ^2 and the Kolmogorov-Smirnov statistic can be used to measure similarities between distributions. However, they estimate maximum deviation or bin-by-bin residuals and are not sufficiently sensitive to the full shape of distributions. Instead, we seek the posterior and the uniform distribution to have close agreement across their full support, not just at a single point or quantile. Therefore, we use the Earth Mover's Distance (EMD; Givens & Shortt 1984) — aka, the Wasserstein distance — to estimate the similarity between the posterior rank histogram and the uniform distribution. EMD quantifies the discrepancy between the two distributions as the minimum cost required to transform one distribution into the other, where cost is defined as the amount of probability mass moved multiplied by the distance it is transported. A small EMD value means that the two distributions are very similar in shape and location: only a small amount of probability mass needs to be transported, and over short distances, to transform one distribution into the other.

To find optimal values of Γ and Δ, our search strategy starts with a Sobol sequence, a quasi-random sampling method designed to cover the Γ-Δ parameter space more uniformly than standard pseudo-random sampling. We adopt broad prior ranges to ensure that the search space encompasses all physically plausible calibration states without truncation at the boundary. These parameters apply a single global correction to the entire prior, so the dataset only needs to be large enough to provide a reliable estimate of the average calibration needed across the full prior space. A much larger calibration dataset would be needed if, instead of a single global correction, one required a spatially varying correction that adapts

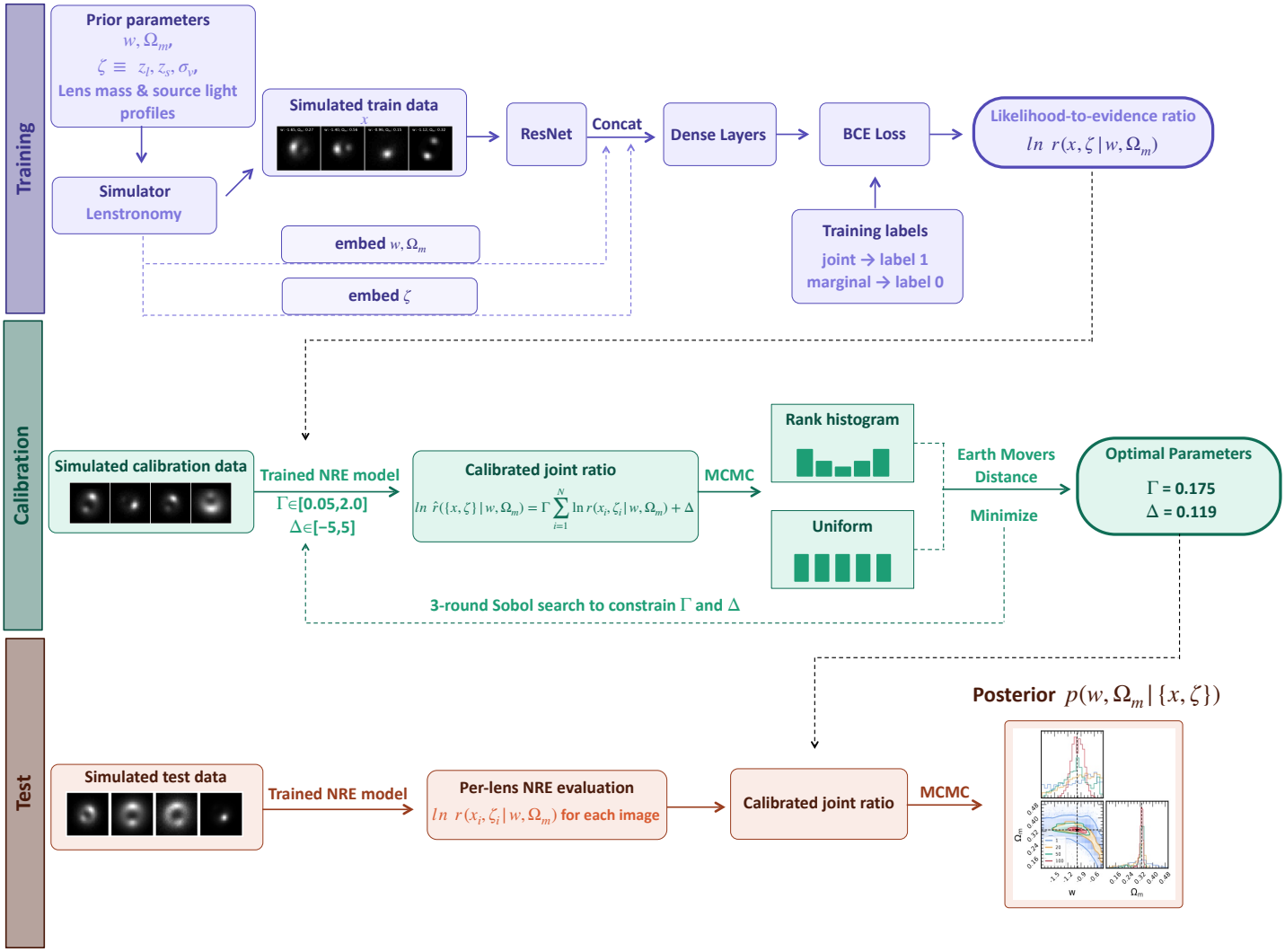

Figure 4. Workflow diagram of the NRE pipeline, including calibration. Top (Training): Simulated images and the corresponding cosmological parameters (w, Ω_m) and astrophysics parameters $(\zeta \equiv z_l, z_s, \sigma_v)$ are inputs for training NRE to generate the LR $\ln r(x, \zeta \mid w, \Omega_m)$. The model architecture and training are discussed in Sec. 4.4 and Appendix A. Middle (Calibration): A three-round Sobol search over scaling parameters Γ and Δ minimizes the Earth Mover's Distance between posterior rank histograms and a uniform distribution. This yields a calibrated population-level log-LR $\ln \hat{r}(\{x, \zeta\} \mid w, \Omega_m) = \Gamma \sum_i \ln r(x_i, \zeta_i \mid w, \Omega_m) + \Delta$. The calibration method is detailed in Sec. 4.3. Bottom (Test): The per-lens log-ratios are obtained from the trained NRE model. The calibration is applied to the summed log-likelihoods and MCMC-sampled to recover the posterior $p(w, \Omega_m \mid \{x, \zeta\})$. The MCMC sampling is described in Sec. 4.1.

to different Sub-Regions of the prior separately. Ideally, one would use a calibration dataset of the same size as the test dataset (100 cosmologies), but the Sobol search is computationally expensive because each candidate (Γ, Δ) pair requires running MCMC chains to construct rank histograms. We use 50 cosmologies as a practical compromise. To find the optimal calibration parameters, we use a held-out calibration dataset with the parameters sampled from the entire training prior of cosmological parameters.

The following algorithm describes the iterative optimization procedure:

Input: Trained NRE model (Eqn. 19); calibration dataset.
Output: Optimal parameters Γ and Δ.

Objective Function Definition:

- Calibrated log-LR (Eqn. 21).
- EMD post hoc calibration loss function $L(\Gamma, \Delta)$.

Round 1: Global Coarse Search

- Sobol sequence: sample $\Gamma \in [0.05, 2.0]$, $\Delta \in [-5.0, 5.0]$.
- For each parameter pair, sample log-LR posteriors (20 lenses per cosmology pair for 50 cosmology pairs, 4 walkers, 10 burn-in, 100 steps).
- Calculate rank histograms from posterior samples.
- Calculate $L(\Gamma, \Delta)$ for parameter pairs.
- Identify top five parameter pairs for $L(\Gamma, \Delta) < 0.3$.

Round 2: Intermediate Refinement

- Reduce Round 1 search space by a factor of 0.4.
- Sample posteriors for each parameter pair (50 lenses per cosmology pair for 50 cosmology pairs, 4 walkers, 20 burn-in, 120 steps).
- Calculate rank histograms from posterior samples.
- Calculate $L(\Gamma, \Delta)$ for parameter pairs.
- Identify top 5 pairs for $L(\Gamma, \Delta) < 0.3$.

Round 3: Fine Optimization

- Reduce Round 2 search space by factor of 0.4 for finer sampling.
- Sample posteriors (100 lenses per cosmology pair for 50 cosmology pairs, 4 walkers, 30 burn-in, 200 steps).
- Calculate rank histograms from posterior samples.
- Calculate $L(\Gamma, \Delta)$ for parameter pairs.
- Result: Optimal parameters at $(\Gamma, \Delta) = (0.175, 0.119)$.

For each Round, the sampling count regards lenses per pair of cosmological parameters. Posterior sampling is performed using MCMC. We apply the optimal values we found $(\Gamma, \Delta) = (0.175, 0.119)$ to the LR during parameter estimation for both the Entire Test Region and individual Sub-Regions.

4.4. *Model Architecture and Training*

We use a ResNet architecture (He et al. 2015), implemented in `TensorFlow` (Abadi et al. 2016). Details of the model architecture are shown in Table 3 in Appendix A. The inputs are images and their cosmology and astrophysics parameters. Samples from the marginal distribution $p(x, \zeta)p(w)p(\Omega_m)$ are generated by pairing each image with randomized values of w and Ω_m. Samples from the joint distribution $p(x, \zeta, w, \Omega_m)$ retain the true generating cosmology parameters. The network outputs a scalar for the logarithm of the LR as detailed in Sec. 4.1 and shown by Eqn. 19. Samples are drawn at the batch level because randomizing at the batch level increases the diversity of the samples from the marginal distribution.

The image input is first passed through batch normalization followed by a convolutional layer with a ReLU activation, serving as the entry block of a residual network. The feature maps are then processed by three residual convolutional blocks with increasing channel width. Each block consists of two 3×3 convolutional layers, each followed by batch normalization and ReLU activation, and a max-pooling layer for spatial downsampling. Residual connections are implemented using projection shortcuts via 1×1 convolutions with matching stride, allowing the network to preserve low-level spatial information while enabling deeper feature extraction. Following the residual blocks, a separable convolutional layer is applied to increase representational capacity at reduced computational cost. Global average pooling is then used to collapse the spatial dimensions, yielding a fixed-length one-dimensional feature vector that summarizes the image content.

The astrophysical parameters ζ and the cosmological parameters (w, Ω_m) are provided to the network as separate inputs. The astrophysical parameters are assumed to be known perfectly (i.e., no error bars) during inference and are provided to the network to reduce the degeneracy between the Einstein radius and the parameters from Eqn. 7. Each of the astrophysics and cosmology parameter vectors is independently normalized using batch normalization and passed through a dense embedding layer to project the parameters into a higher-dimensional latent feature space. The embedded astrophysical features and cosmological features are concatenated with the image feature vector after global average pooling. The concatenated feature vector is processed by a sequence of fully connected layers with batch normalization and ReLU activations. L2 weight regularization and dropout factor of 0.1 are applied to reduce overfitting and improve generalization. The final linear output layer produces a single scalar corresponding to the logarithmic density ratio.

The model is trained over 100 epochs with a batch size of 1024 using `Adam` optimizer. The learning rate is dynamically adjusted: when the validation loss is plateaued by a decay factor of 0.1, starting from $1e^{-2}$ to $1e^{-6}$, if the validation loss does not improve over five epochs. We use early stopping if the validation loss does not improve over 20 epochs. The model is trained

on NVIDIA A100 GPU with $\sim$ 2M lens images for 80 epochs with a typical training time of $\sim$ three hours.

5. RESULTS: COSMOLOGICAL CONSTRAINTS

We describe the NRE model performance in producing cosmological constraints from individual lenses and populations of lenses. In each scenario, we compare performance without and with the post hoc calibration procedure.

5.1. *Constraints from Individual Lenses*

Each lensing system is simulated using different astrophysical parameters but the same cosmology parameters ($w = -0.99$ and $\Omega_m = 0.33$). Fig. 5 shows images and posteriors obtained from NRE with and without the post hoc calibration. With calibration, the posteriors broaden significantly for Ω_m and less so for w. With or without calibration, the capacity for individual lenses to constrain the cosmological parameters is relatively limited.

5.2. *Constraints from Lens Populations*

We describe the cosmology constraints from NRE-based population-level inference with multiple diagnostics: corner plots, parity (1-1) plots, rank histograms, posterior coverage, and the Earth Mover's Distance (EMD). Unless otherwise stated, these analyses are performed on data from the Entire Test Region (see Fig. 3). The main results are discussed in this section, and additional details from each Sub-Region are discussed in Appendix B.

5.2.1. *Basic Diagnostics*

First, we study the cosmological constraints as function of increasing test set size – one, 20, 50, and 100 lenses. This relates most directly to the main hypothesis of this work: populations of lenses can provide constraints on cosmological parameters. Each test set has the same true cosmological parameters (w = -0.99 and Ω_m = 0.33). Objects in each test set are re-sampled from the astrophysical parameter prior distributions. Several trends appear in Fig. 6. For a single lens, regardless of calibration status, NRE provides no constraint on w, but a small constraint on Ω_m. Then, as the test set size increases, the posterior widths and error bars on both cosmological parameters decrease. For all test set sizes, the posterior widths are wider with calibration than without calibration.

Second, we review posteriors of w and Ω_m from a random sample of nine cosmology parameters. Each panel in Fig. 7 shows the posterior obtained from population-level inference on 100 lenses – each set has a different true cosmological parameter pair. The posteriors without calibration place the true cosmology outside the 68th percentile interval in five of the samples. The posteriors with calibration are broader and place three of the samples outside the 68th percentile interval. Appendix B shows how the model performance varies across Sub-Regions in the cosmological parameter space: the inclusion of the true cosmology in the 68th percentile interval (without or with calibration) varies by Sub-Region.

Third, we study the model accuracy and outliers. The top panels of Fig. 8 present the parity of the predicted values. Without calibration, most median values for w are near parity (the one-to-one line). Some values are far above the parity line and have the same value ($w \sim -0.4$) – the edge of the MCMC sampling prior; most of these values have very small error bars. With calibration, there are only a few such outliers, and they have larger error bars. Without calibration, most median values for Ω_m are near parity. Several values lie systematically below the parity line, and most have negligible error bars. With calibration, fewer points for Ω_m lie below parity. The bottom panels show the residuals of the median values for each parameter of the predicted posteriors with and without calibration. The residuals corroborate the interpretation of the parity plots, and they show more succinctly the quantity and extremity of the outliers. For each of the 100 test cosmologies i from the Entire Test Region, we summarise the 1D marginal posterior of a parameter by its median m_i and the half-width of its 68% credible interval, $\sigma_i = (q_i^{84} - q_i^{16})/2$, where q_i^{16} and q_i^{84} are the 16th and 84th percentiles of the marginal posterior for cosmology i (Fig. 8). We define the fractional uncertainty as $\sigma_i/|m_i|$. Taking the median of this quantity across the 100 test cosmologies, median$(\sigma_i/|m_i|)$ yields 22.8% in w and 2.9% in Ω_m. The calibrated NRE therefore constrains Ω_m roughly eight times more tightly than w, indicating that the matter density is well determined while the dark-energy equation of state is comparatively poorly constrained, as expected given the weaker sensitivity of the data to w. We note that these values quantify precision only; the reliability of the corresponding credible intervals is established by the posterior coverage discussed in Section 5.2.2.

5.2.2. *Posterior Coverage Calibration*

We study the NRE model calibration with diagnostics from SBC, which centers on the posterior coverage and which is the primary arbiter of model efficacy for this work. First, Fig. 9 shows the rank histograms of the posterior samples without and with calibration (blue and orange, respectively). The histogram without calibra-

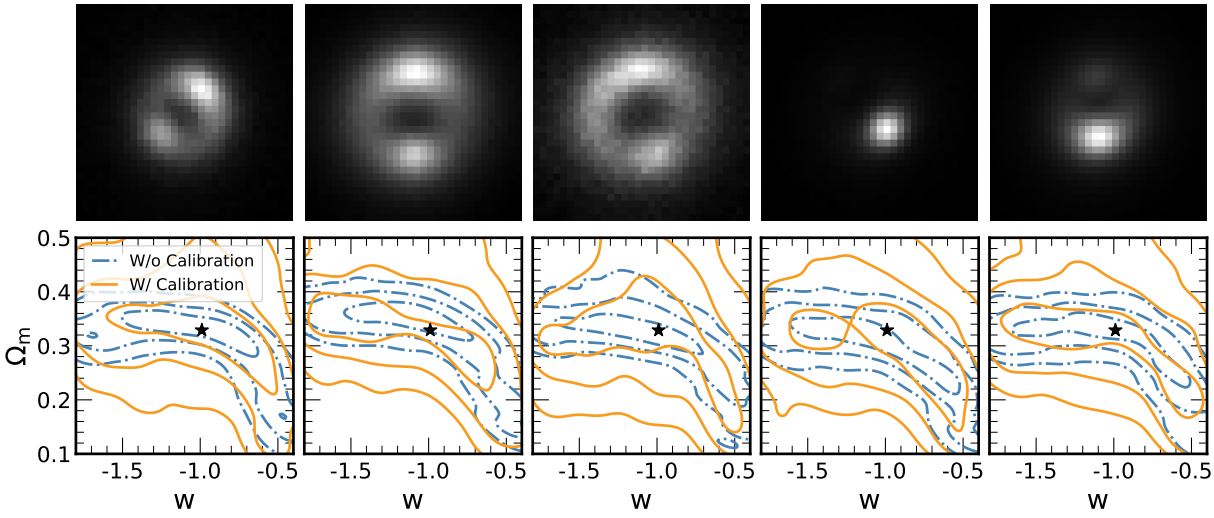

Figure 5. Examples of lensing system images and NRE-based cosmological inferences from those images. All lenses have the same cosmology $w = -0.99$ and $\Omega_m = 0.33$, but different astrophysical parameters. Top: Images of lensing systems, where the lens galaxies have been removed. Bottom: Joint posterior from NRE without calibration (blue, dot-dashed) and with calibration (orange, solid). The contours represent 68th, 95th, and 98th percentile. The true cosmological parameters are denoted with a star.

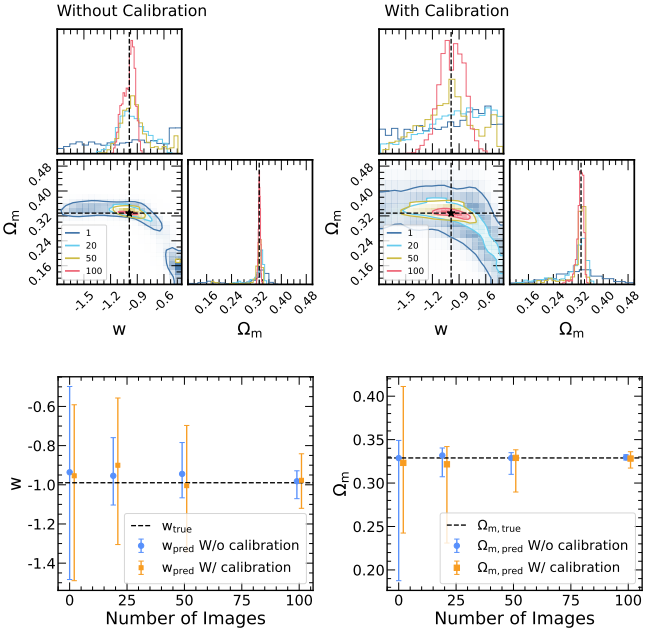

Figure 6. Top: Population-level inference of cosmology parameters without calibration (left) and with calibration (right). The contours are at the 68th confidence percentile. Inference is performed for one (blue), 20 (cyan), 50 (yellow), and 100 (red) lenses. Bottom : Medians of predicted parameter posteriors of w and Ω_m with 68th percentile intervals as a function of the number of images in the test set.

tion is ∪-shaped, indicating over-confident posteriors; the model with calibration is closer to uniform. We use the EMD to examine the difference between the posterior histograms and the uniform distribution for models without and with calibration (Table 2). With calibration, the EMD is lower, indicating that the model produces posteriors closer to the true posterior distribution. Second, for each parameter, we plot the posterior coverage – the fraction of the lenses whose true parameter values fall within a confidence interval as a function of the confidence interval (see Fig. 10). The model without calibration produces over-confident posteriors, and the calibration procedure partially mitigates the overconfidence. The calibrated curves are mostly within 10% tolerance.

We also reviewed individual Sub-Regions without and with calibration. In all Sub-Regions, the post-hoc calibration broadens the posteriors, yielding more conservative uncertainty estimates. In most of the Sub-Regions, there are no more major outliers, the posterior coverage is improved, and the EMD is lower with calibration (see Table 2): the model is no long catastrophically misspecified. However, in some Sub-Regions, the EMD increases with calibration for one of the parameters (and in one of the Sub-Regions for both parameters). A more detailed discussion of the Sub-Region results is presented in Appendix B.

6. DISCUSSION

We study the NRE model performance as a function of training set size, perform a comparison to analytic-based methods, and review the post hoc calibration consistency across Sub-Regions of the test parameter space.

6.1. *Effect of training set size*

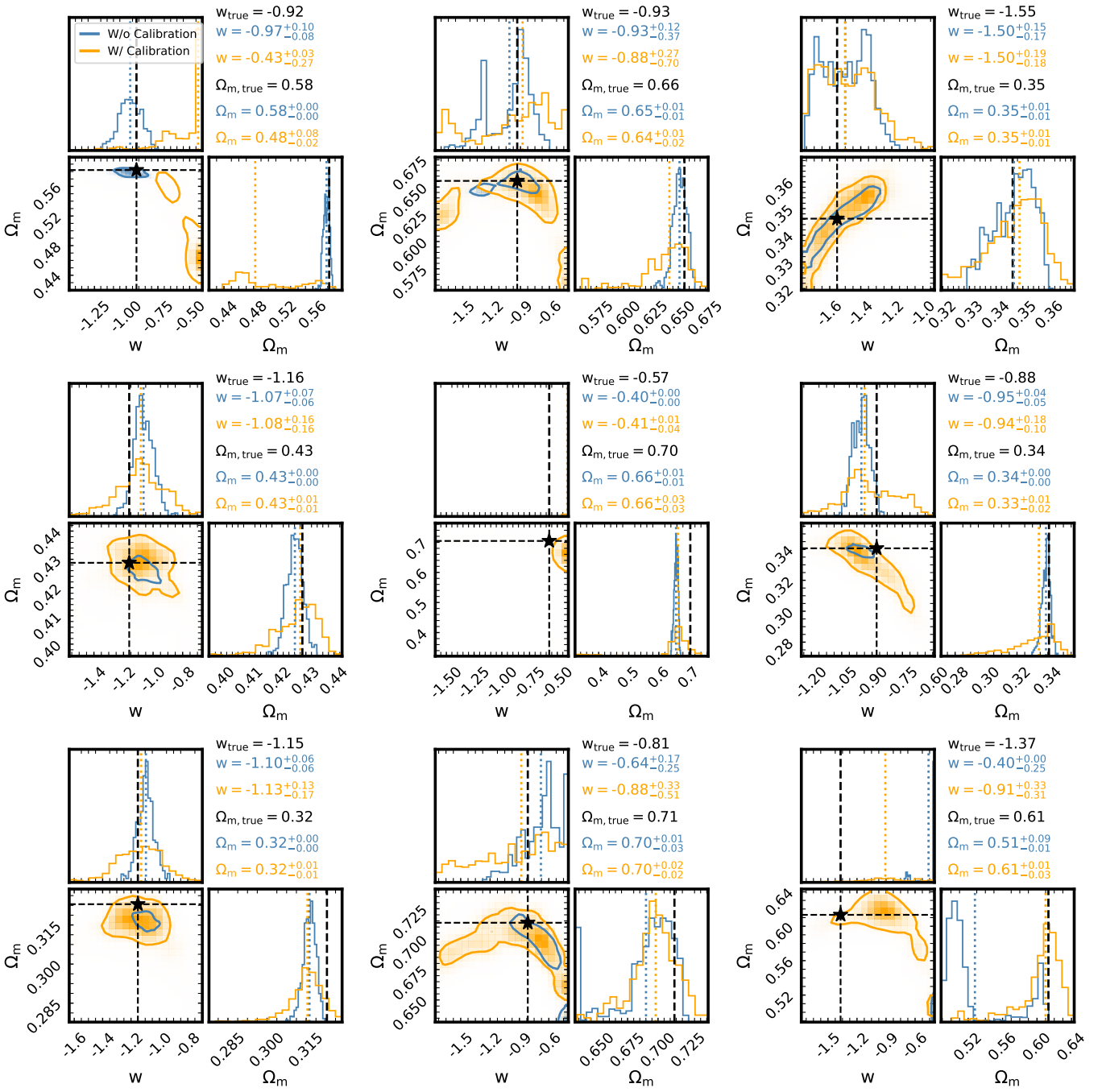

Figure 7. NRE-based posteriors – without calibration (blue) and with calibration (orange) of nine pairs of cosmological parameters randomly selected from the Entire Test Region. Each example uses 100 objects with the same true cosmology parameters (black star). The contours in the joint posteriors represent the 68th percentile. The histograms represent the marginal posterior and show the median (dotted line) and the true value (dashed black line).

One possible explanation for the overconfidence observed in the uncalibrated NRE posteriors (Sec. 5.2) is insufficient training data: a classifier trained on few examples may learn a decision boundary that does not generalize. We test this hypothesis by training four models on datasets of ∼500K, ∼1M, ∼1.5M, and ∼2M lens images. The lens, source, and cosmology parameters are drawn from the same prior distributions (Table 1). The models are evaluated on the same held-out test dataset generated from the Entire Test Region prior range comprising 100 distinct cosmologies, with 100 lens images generated per cosmology.

Fig. 11 shows the predicted median and 68% credible intervals for 100 cosmologies sampled from the Entire

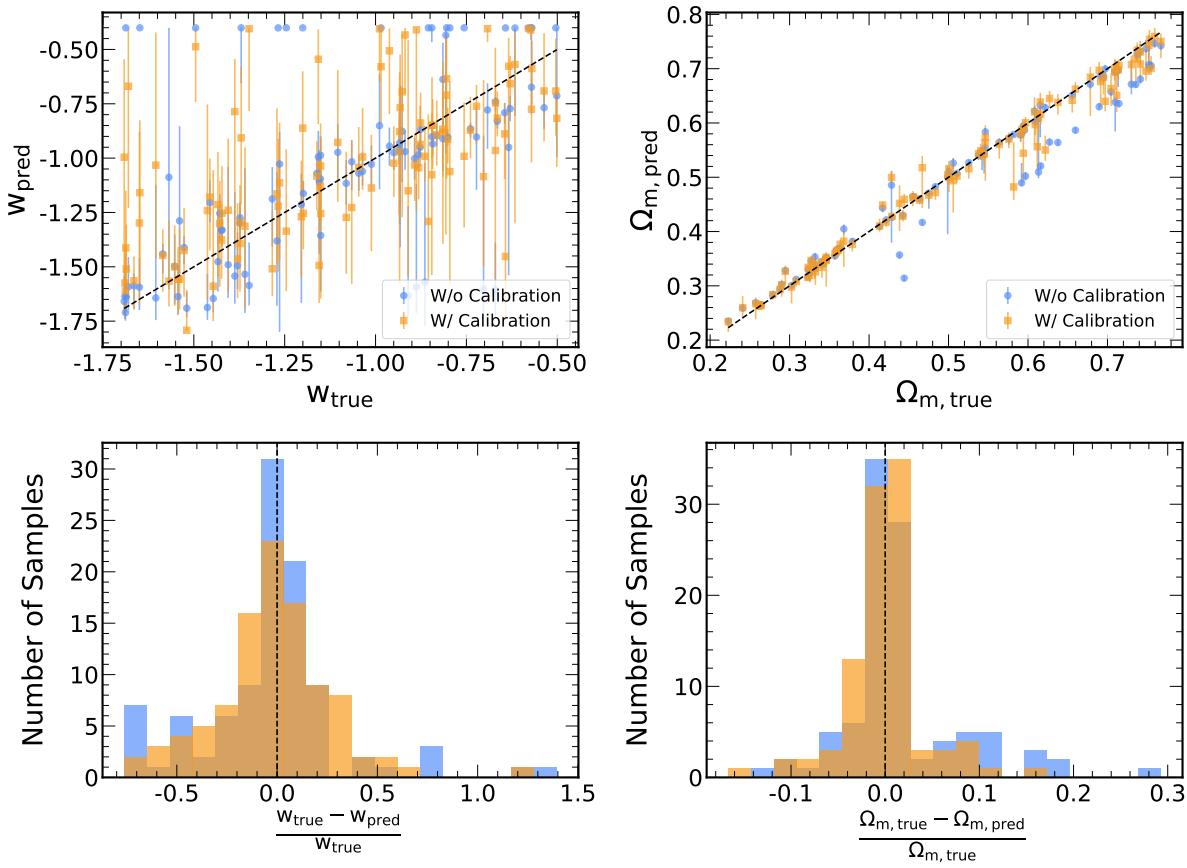

Figure 8. Top: True and predicted median values of w (left) and Ω_m (right) from population-level posteriors for 100 cosmologies, with 100 lenses per cosmology. The error bars represent the 16th and 84th percentile values. Bottom: The residuals of the predicted median values of the posteriors. Posteriors without calibration are shown in blue, and those with calibration are shown in orange.

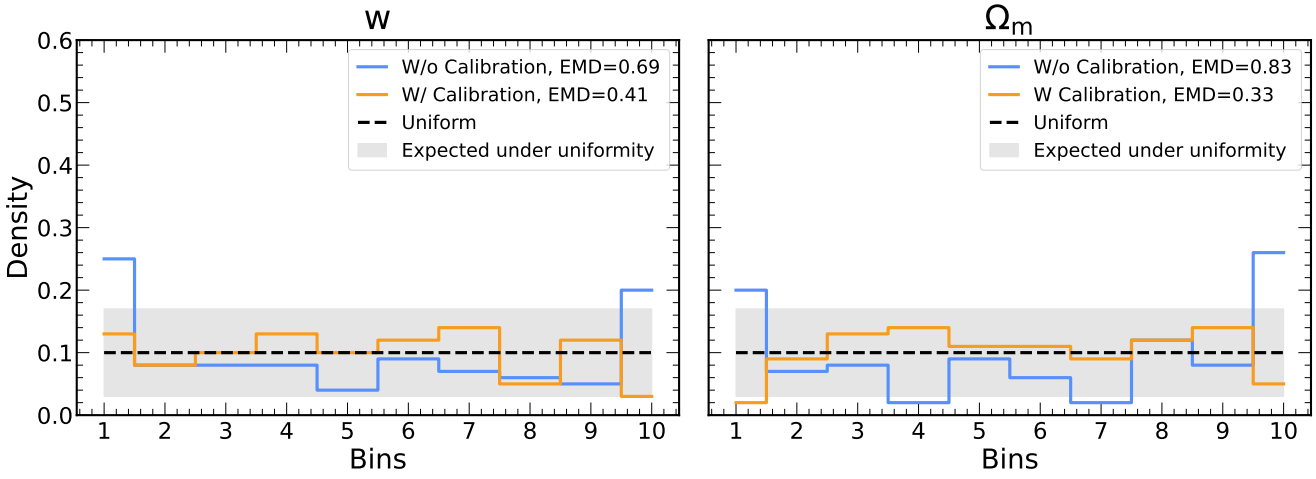

Figure 9. Rank histograms of the posteriors of w (left) and Ω_m (right) without (blue) and with (orange) calibration. The uniform distribution is shown with a black dashed line. The 99%-confidence interval is shown in gray. EMD values without and with calibration are shown in the legend.

Test Region prior, along with the residuals, for each training set size. Increasing the training sample by a

Table 2. Priors and Earth Mover's Distance (EMD) for w and Ω_m in the Entire Test Region and in each Sub-Region without (w/o) and with (w/) calibration.

	Priors		EMD_w		EMD_{Ω_m}	
Region	w	Ω_m	(w/o)	(w/)	(w/o)	(w/)
Entire Region	$\mathcal{U}(-1.70, -0.50)$	$\mathcal{U}(0.22, 0.77)$	0.69	0.41	0.83	0.33
Sub-Region 1	$\mathcal{U}(-1.70, -1.50)$	$\mathcal{U}(0.22, 0.38)$	1.80	1.13	1.81	1.07
Sub-Region 2	$\mathcal{U}(-1.10, -0.90)$	$\mathcal{U}(0.22, 0.38)$	1.67	1.44	0.46	0.41
Sub-Region 3	$\mathcal{U}(-0.70, -0.50)$	$\mathcal{U}(0.22, 0.38)$	3.19	1.44	3.19	1.35
Sub-Region 4	$\mathcal{U}(-1.70, -1.50)$	$\mathcal{U}(0.42, 0.57)$	0.18	0.77	0.30	0.76
Sub-Region 5	$\mathcal{U}(-1.10, -0.90)$	$\mathcal{U}(0.42, 0.57)$	0.57	1.00	1.96	1.08
Sub-Region 6	$\mathcal{U}(-0.70, -0.50)$	$\mathcal{U}(0.42, 0.57)$	1.72	1.69	1.56	1.57
Sub-Region 7	$\mathcal{U}(-1.70, -1.50)$	$\mathcal{U}(0.62, 0.77)$	1.71	1.70	1.44	1.70
Sub-Region 8	$\mathcal{U}(-1.10, -0.90)$	$\mathcal{U}(0.62, 0.77)$	1.58	0.44	3.00	1.63
Sub-Region 9	$\mathcal{U}(-1.70, -1.50)$	$\mathcal{U}(0.62, 0.77)$	0.81	1.31	1.41	0.41

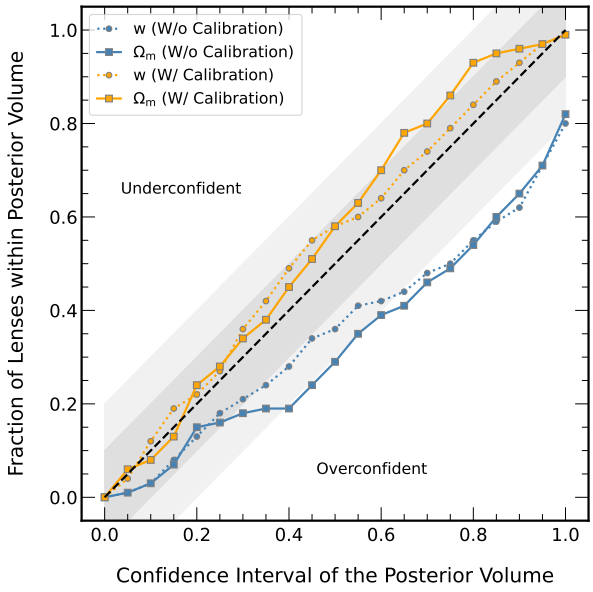

Figure 10. The posterior coverage from 100 cosmologies sampled from the Entire Test Region, with 100 lenses per cosmology. Blue (orange) curves show the model performance without (with) calibration. The dark- and light-gray shaded bands around the diagonal denote 10% and 20% thresholds, respectively.

factor of four produces no detectable reduction in overconfidence, though we cannot rule out that increases of an order of magnitude or more may be required to see a significant effect. Post-hoc calibration therefore remains a practical requirement of the framework at the training set sizes explored here.

6.2. *Comparing NRE-based and analytic methods*

We compare our calibrated NRE likelihood with two implementations of the analytic approach – one that we perform and one from the literature. Generally, all methods follow the same population-level Bayesian framework where individual per-lens likelihoods are combined and the joint posterior over w and Ω_m is sampled via MCMC (Sec. 4.1).

The efficacy of traditional analytical likelihood methods is tied to the chosen model's capacity to represent the physical complexities of the data. In our analytical implementation, we assume a simple SIE lens profile to estimate the Einstein radius, representing the lens image. Given a candidate cosmology (w, Ω_m) and the known astrophysical parameters ζ_i for that lens, the predicted Einstein radius $\hat{\theta}_{E,i}$ is computed from Eqn. 7. The analytical log-likelihood for the population is then

$$p(x|w, \Omega_m) = \sum_{i=1}^{N} (\theta_{E,i} - \hat{\theta}_{E,i})^2. \tag{22}$$

Fig. 12 compares the resulting population-level posteriors. The calibrated NRE likelihood yields well-constrained posteriors for both w and Ω_m (red curves). The analytic approach fails to constrain w and produces a broad constraint on Ω_m (gray curves).

Alternatively, a more realistic lens profile may give a more accurate description of strong lens systems. In contrast to the SIE lens profile assumptions in this study, Li et al. (2024) employ an analytic hierarchical Bayesian framework using a power-law mass profile and stellar luminosity to simultaneously constrain the lens population and cosmological parameters. They use a cosmology with true parameters $w = -1.0$ and $\Omega_m = 0.3$. From 10,000 mock observations, they recover $w = -0.98 \pm 0.11$ and $\Omega_m = 0.300 \pm 0.015$. Applying our work's calibrated NRE approach to 100 simulated lens images with true cosmology $w = -0.99$ and $\Omega_m = 0.33$, we obtain $w = -1.01 \pm 0.39$ and $\Omega_m = 0.39 \pm 0.10$. We evaluate and compare the reliability of these predictions using the

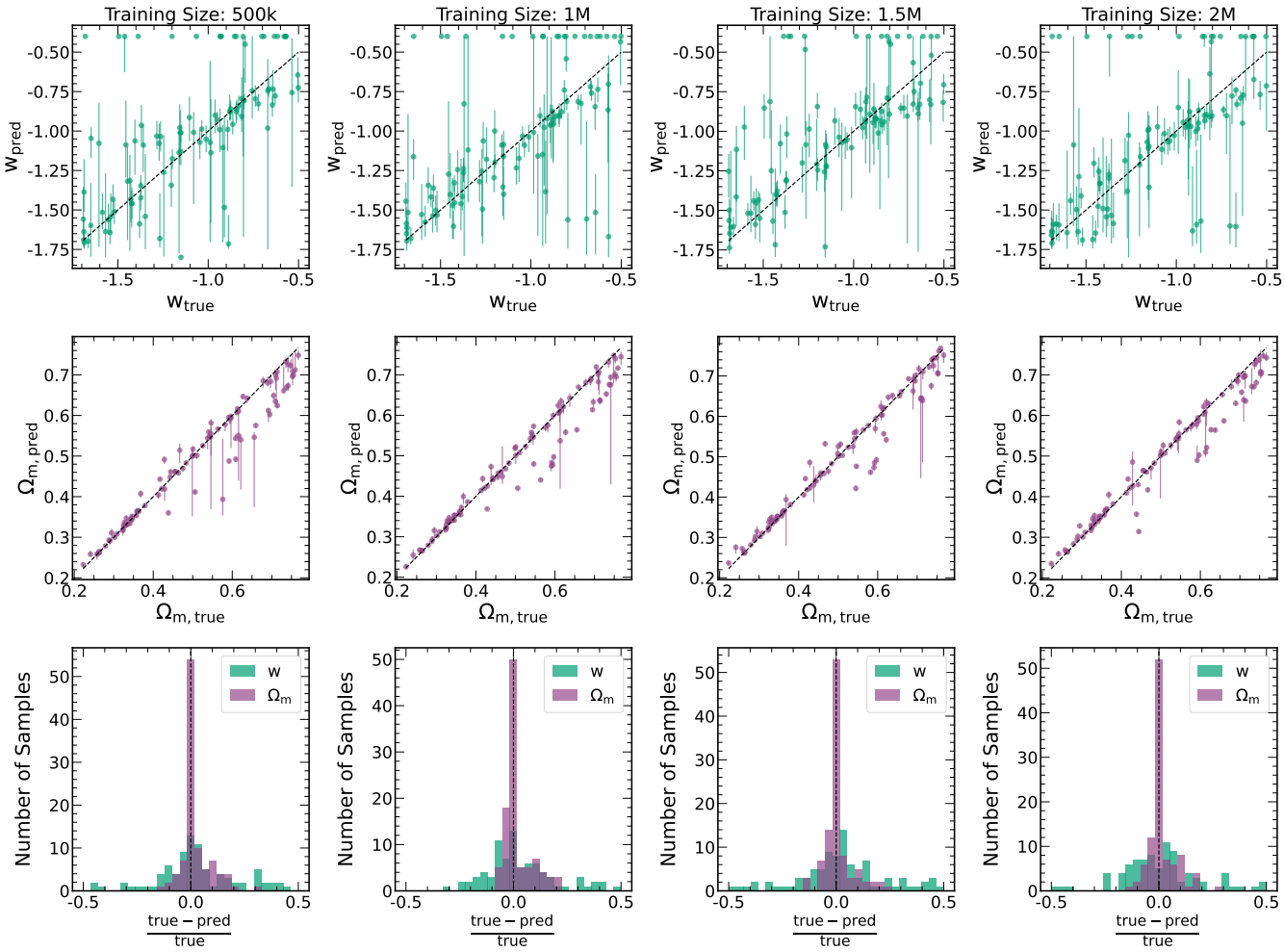

Figure 11. Model performance (before calibration) as a function of training set size (from left to right: 500K, 1M, 1.5M, and 2M). Top (green): parity (predicted vs. true) of the median value of the predicted posterior of w for 100 cosmologies, each with 100 objects sampled from the Entire Test Region. The error bars indicate the 16th and 84th percentile intervals, centered on the median. Middle (violet): same as top row, but for Ω_m. Bottom: residuals of the median values of predicted posteriors for each cosmological parameter.

Z-score, which measures the distance between the predicted mean ($\hat{\theta_\mu}$) and the ground truth (θ) in units of the predicted standard deviation ($\hat{\theta_\sigma}$): $Z = \frac{\hat{\theta_\mu} - \theta}{\hat{\theta_\sigma}}$. This is also considered as the number of standard deviations that the predicted mean lies from the true value. A Z-score close to 0 indicates high agreement, and values within ± 1 are considered good. The analytical approach by Li et al. (2024) yields $Z_w = 0.18$ and $Z_{\Omega_m} = 0.00$, and our NRE-based inference yields $Z_w = -0.05$ and $Z_{\Omega_m} = 0.60$. All scores fall within ± 1, both methodologies are considered statistically reliable. The NRE model uses a sample size 100 times smaller than that required by Li et al. (2024).

6.3. *Sub-Region calibration consistency*

Our calibration procedure aims to minimize the EMD between posterior rank distributions and a uniform distribution by re-scaling the joint LR across the w-Ω_m parameter space. The re-scaling is determined by Eqn. 21, where the parameters Γ and Δ are optimized by a held-out calibration data set across the parameter space. The resulting calibration produces posteriors across the Entire Test Region that are reduced from overconfident to moderately underconfident (see Fig. 10). However, models in individual test Sub-Regions are affected differently: for example, while most models become either well-calibrated or underconfident for both cosmological parameters, some models are more overconfident in one parameter and slightly underconfident in another. Consider Sub-Region 5, where the coverage curve after calibration is S-shaped in Ω_m indicating that the posterior

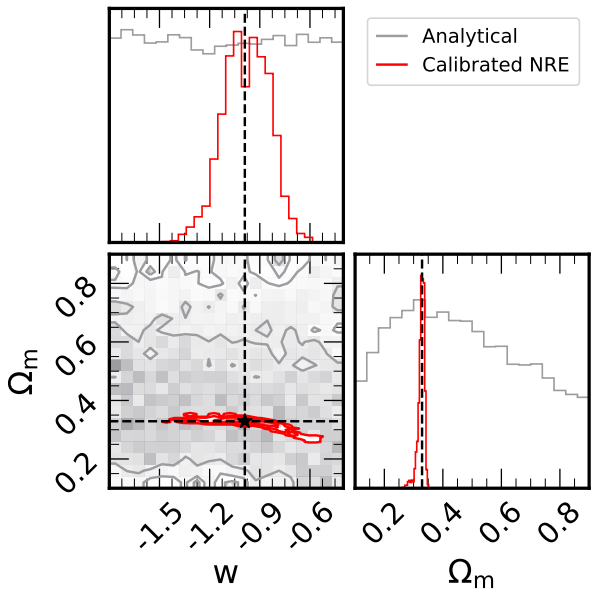

Figure 12. Comparison between the posteriors calculated from an analytic likelihood (gray) with those from an NRE-based likelihood (red). True values for w and Ω_m are marked with a dashed line.

is overconfident in the centre and underconfident in the tails. Similarly, in Sub-Regions 7 and 8, models remain significantly overconfident in w and slightly underconfident in Ω_m, respectively, but no longer catastrophically misspecified.

More detailed analysis of the model behavior in all Sub-Regions, with the corresponding, figures can be found in Appendix B. Future work will focus on uncovering the causes and mitigating the variable efficacy of calibration in all Sub-Regions.

7. CONCLUSION

In this work, we presented the first NRE-based population-level inference of w and Ω_m from galaxy-galaxy strong lensing images. The main conclusions in this study are:

- NRE (without or with a calibration procedure) produces very limited constraints based on individual lensing systems (Fig.'s 5 and 6). This is true especially for w. Ω_m can still be somewhat constrained from a single lens.

- NRE (without or with a calibration procedure) produces tighter constraints when invoked for population-level inference (Fig. 6): the size of the posterior contours decreases as the number of objects in the tested population increases.

- NRE without calibration produces overconfident posteriors for individual and population-level inference. We used a post hoc calibration procedure that aims to reduce the confidence (increase the posterior width). The calibration performance depends on the region of parameter space where the inference is taking place. This calibration mitigates overconfidence throughout most of the parameter space that we tested (Fig.'s 5, 6, 7, 8, 9, and 10).

- There does not appear to be a change in performance of the NRE approach when training sizes are increased from 500k to 2M, which is less than order of magnitude (Fig. 11).

- The calibrated NRE model has a Z-score comparable to analytic likelihood on simulated data from Li et al. (2024); see Sec. 6.2.

- We have not yet uncovered the cause of variable efficacy of the calibration from Sub-Region to Sub-Region or what allows the calibration to succeed for the Entire Test Region, while not consistently successfully across the Sub-Regions. This is the next major step for future studies.

Recall the context, assumptions, and caveats for this proof-of-concept study. First, we performed experiments on data simulated to mimic ideal lensing systems: the idealization pertains to redshift and morphological configurations and to DES observational noise, primarily regarding pixel scale and exposure time. We also assume perfect lens light subtraction and perfect deblending. Additionally, the present analysis is limited to g-band imaging. Incorporating multi-band photometry in future work would provide richer color information, reduce degeneracies between lens and source parameters, potentially allowing for stronger cosmological constraints.

Second, we treat the astrophysical parameters z_l, z_s, and σ_v as perfectly measured, ignoring observational uncertainties. In practice, these quantities carry non-negligible measurement errors and their observation typically requires significant experimental effort beyond photometric survey imaging. Incorporating these uncertainties in future studies would enhance the realism of cosmological constraint estimates derived from NRE-based population-level inference.

Third, the present study aims to derive constraints over a large, uniformly sampled parameter space (Entire Test Region); some Sub-Regions may require denser sampling for the algorithm to learn accurately and consistently across that large space. Similarly, this under-

dense sampling may be the cause of the non-uniformity of the calibration in specific parameter Sub-Regions. Furthermore, the MCMC search strategy for the calibration is computationally expensive and sensitive to the initial conditions leading to possible convergence on local optima. These computational inefficiencies may be mitigated by a secondary neural network that uses the data to predict the scaling factors for the calibration. Alternatively, replacing the current staged search with a more sample-efficient approach, like Bayesian Optimization, may improve convergence efficiency.

Finally, bridging the gap between simulations and real observations is an active area of research in the field. Promising approaches include domain adaptation techniques that align the feature distributions of simulated and observed data (e.g., Ćiprijanović et al. 2023; Pandya et al. 2025; Treyer et al. 2026), and nuisance-randomized training strategies that render the inference robust to nuisance variables (e.g., Puli et al. 2021; Gandrakota et al. 2024).

In this study, we have taken initial steps toward demonstrating the potential of NRE for population-level inference in a cosmological context. The next, primary quandary to address is the inconsistency of the model calibration and performance across the w-Ω_m parameter space. This would begin with an investigation of objects in the Sub-Regions where calibration was less successful. After addressing and mitigating inconsistencies, assumptions, and caveats, future work may be able to use NRE to derive state-of-the-art constraints from strong lens populations observed with Rubin, Euclid and Roman.

ACKNOWLEDGMENTS

Funding: This work was produced by Fermi Forward Discovery Group, LLC under Contract No. 89243024CSC000002 with the U.S. Department of Energy, Office of Science, Office of High Energy Physics. Publisher acknowledges the U.S. Government license to provide public access under the DOE Public Access Plan DOE Public Access Plan (http://energy.gov/downloads/doe-public-access-plan).

The work of S.J. and B.N. (while at Fermilab) was supported by the DOE Grant No. 0000258217 (FNAL 21-25).

Author Contributions:

Jarugula: Methodology, Formal analysis, Software, Validation, Data curation, Writing - Original draft.

Nord: Conceptualization, Methodology, Writing - Review & Editing (including AI-removal editing), Supervision, Project administration, Funding acquisition. Nord did not use AI in the writing or editing of this manuscript.

Ćiprijanović: Methodology, Writing - Review & Editing, Supervision, Project administration.

Trivedi: Methodology, Writing - Review & Editing.

AI Disclosure: The generative AI tool Claude Sonnet 4.6 was used in the preparation of this manuscript. The Abstract, Introduction, Sec.s 6.2 and 6.3, and the Conclusion were drafted by the authors and polished with the help of AI; they were then rewritten by humans, attempting to remove the influence of AI. Claude was used to generate the algorithm table in Sec. 4.2 in LaTeX format. Claude was used to edit the code for visualization (layout and formatting of Fig.'s 5, 7, and 11) and the code for the calibration. It was also used to assist in identifying statistical metrics for comparing posterior distributions with literature values; this led to the use of the Z-score. The interpretation of all calculations (including the Z-score) was performed by the authors. Finally, authors who did not use AI performed a final pass through the full manuscript to rewrite or significantly edit the sections where AI was used.

Software: `astropy` (Astropy Collaboration et al. 2013, 2018), `deeplenstronomy` (Morgan et al. 2021), `lenstronomy` (Birrer et al. 2015; Birrer & Amara 2018).

APPENDIX

A. NETWORK ARCHITECTURE

Layer Type	Output Shape	No. of Parameters
Input Images x	(Batch, 32, 32, 1)	0
Conv2D (3×3, stride 2, 8 filters)	(Batch, 16, 16, 8)	$3{\times}3{\times}1{\times}8 + 8 = 80$
Residual Block 1 (16 filters)		
Conv2D (3×3)	(Batch, 16, 16, 16)	$3{\times}3{\times}8{\times}16 + 16 = 1{,}168$
Conv2D (3×3)	(Batch, 16, 16, 16)	$3{\times}3{\times}16{\times}16 + 16 = 2{,}320$
MaxPooling (stride 2)	(Batch, 8, 8, 16)	0
Residual Projection Conv2D (1×1, stride 2)	(Batch, 8, 8, 16)	$1{\times}1{\times}8{\times}16 + 16 = 144$
Add	(Batch, 8, 8, 16)	$0 \leftarrow$
Residual Block 2 (32 filters)		
Conv2D (3×3)	(Batch, 8, 8, 32)	$3{\times}3{\times}16{\times}32 + 32 = 4{,}640$
Conv2D (3×3)	(Batch, 8, 8, 32)	$3{\times}3{\times}32{\times}32 + 32 = 9{,}248$
MaxPooling (stride 2)	(Batch, 4, 4, 32)	0
Residual Projection Conv2D (1×1, stride 2)	(Batch, 4, 4, 32)	$1{\times}1{\times}16{\times}32 + 32 = 544$
Add	(Batch, 4, 4, 32)	$0 \leftarrow$
Residual Block 3 (45 filters)		
Conv2D (3×3)	(Batch, 4, 4, 45)	$3{\times}3{\times}32{\times}45 + 45 = 13{,}005$
Conv2D (3×3)	(Batch, 4, 4, 45)	$3{\times}3{\times}45{\times}45 + 45 = 18{,}270$
MaxPooling (stride 2)	(Batch, 2, 2, 45)	0
Residual Projection Conv2D (1×1, stride 2)	(Batch, 2, 2, 45)	$1{\times}1{\times}32{\times}45 + 45 = 1{,}485$
Add	(Batch, 2, 2, 45)	$0 \leftarrow$
SeparableConv2D (3×3, 64 filters)	(Batch, 2, 2, 64)	$3{\times}3{\times}45 + 45{\times}64 + 64 = 3{,}349$
Global Average Pooling (Embedding A)	(Batch, 64)	0
Input Astrophysics Params ($z_{\rm l}, z_{\rm s}, \sigma_{\rm v}$)	(Batch, 3)	0
Dense Embedding (Embedding B)	(Batch, 64)	$3{\times}64 + 64 = 256$
Input Cosmology Params (w,Ω_m)	(Batch, 2)	0
Dense Embedding (Embedding C)	(Batch, 64)	$2{\times}64 + 64 = 192$
Concatenate Embeddings A, B, C	(Batch, 192)	0
Dense	(Batch, 192)	$192{\times}192 + 192 = 37{,}056$
Dropout	(Batch, 192)	0
Dense	(Batch, 64)	$192{\times}64 + 64 = 12{,}352$
Dropout	(Batch, 64)	0
Dense ($\ln r$)	(Batch, 1)	$64{\times}1 + 1 = 65$

Table 3. Summary of the NRE network architecture with output shapes and parameter counts for $32 \times 32 \times 1$ input images. Residual skip connections are indicated by the arrows and implemented through projection shortcuts and *Add* layers. Batch normalization and activation functions are applied after each convolutional and dense layer.

B. MODEL PERFORMANCE IN TEST SUB-REGIONS

We report on NRE model performance in each of the test Sub-Regions. These figures may be compared with those in Sec. 5, where we analyze the Entire Test Region. The post hoc calibration was trained using data from the Entire Test Region of the test data and applied to each Sub-Region individually. This analysis provides information regarding which Sub-Regions could be better calibrated with the post hoc procedure. Investigations into the causes of the more and less successful calibrations (by Sub-Region) will likely aid in determining how to improve the procedure for the Entire Test Region.

B.1. *Sub-Region 1*

Posterior Contours (Fig. 13): Posteriors are larger with calibration (orange) than without calibration (blue); all posteriors with calibration contain the true points, but one posterior without calibration excludes the true value.

Parity and Residuals (Fig. 14): Median w values are much higher and median Ω_m values are slightly higher than truth both with and without calibration

Rank Histogram (Fig. 15): Histograms for both w and Ω_m are left-skewed without calibration, and less so with calibration. The EMD is lowered but nonzero with calibration.

Posterior Coverage (Fig. 16): For both parameters, the model is partially overconfident without calibration; it is fully underconfident with calibration.

For w, with calibration, the model is made less biased and underconfident. For Ω_m, with calibration, the model bias is left unchanged, and it is made underconfident.

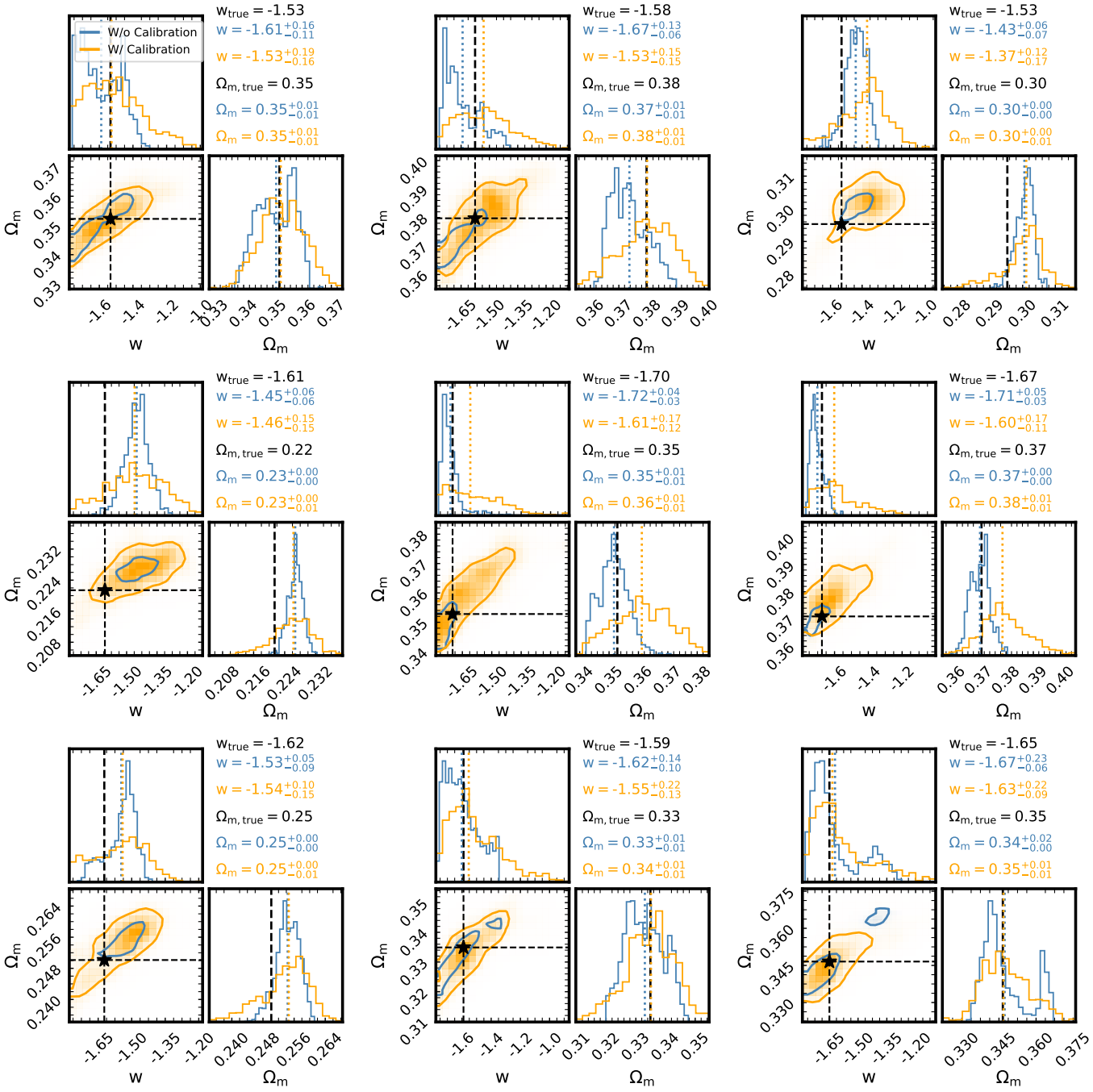

Figure 13. Same as Fig. 7, but for Sub-Region 1.

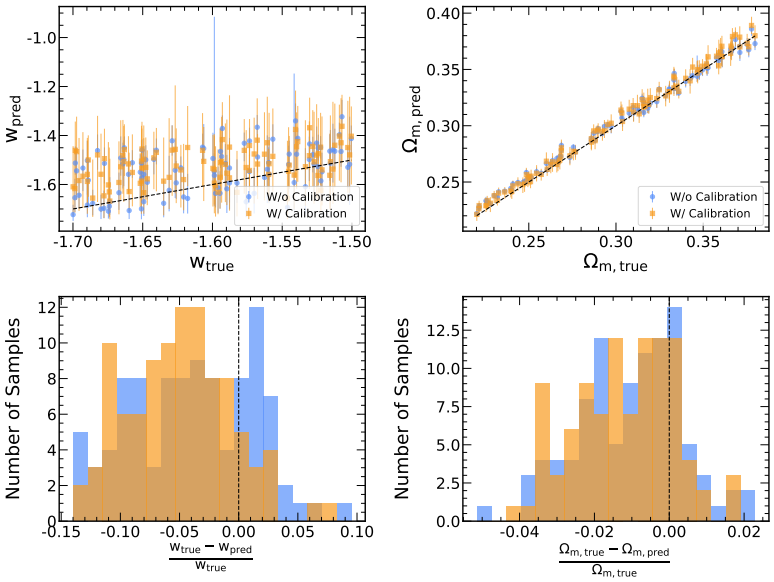

Figure 14. Same as Fig. 8, but for Sub-Region 1.

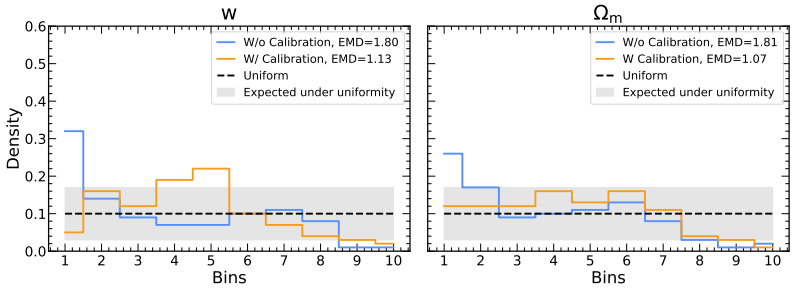

Figure 15. Same as Fig. 9, but for Sub-Region 1.

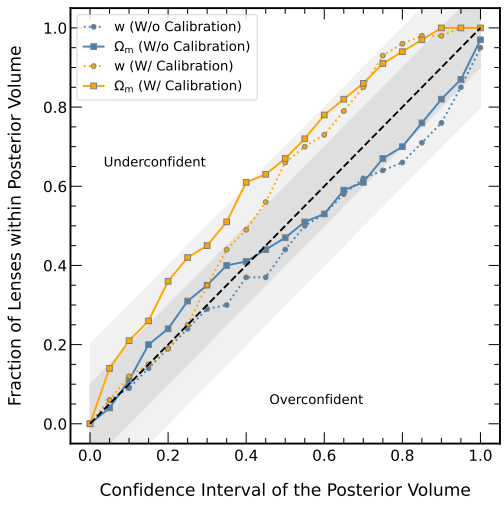

Figure 16. Same as Fig. 10, but for Sub-Region 1.

B.2. *Sub-Region 2*

Posterior Contours (Fig. 17): The contours are larger with calibration than without calibration; contours in both scenarios contain the true values.

Parity and Residuals (Fig. 18): With and without calibration, the median w values are lower than truth, and the median Ω_m values are near truth.

Rank Histogram (Fig. 19): With and without calibration, the w ranks are right-skewed; Ω_m is consistent with uniform. The EMD for w is lower with calibration; Ω_m same with and without calibration.

Posterior Coverage (Fig. 20): With calibration, the model becomes highly underconfident for both parameters.

The model accuracy is unchanged with calibration. For w, the model confidence is lessened from almost perfect to significantly underconfident; for Ω_m, the model confidence is lessened from partially overconfident to significantly underconfident.

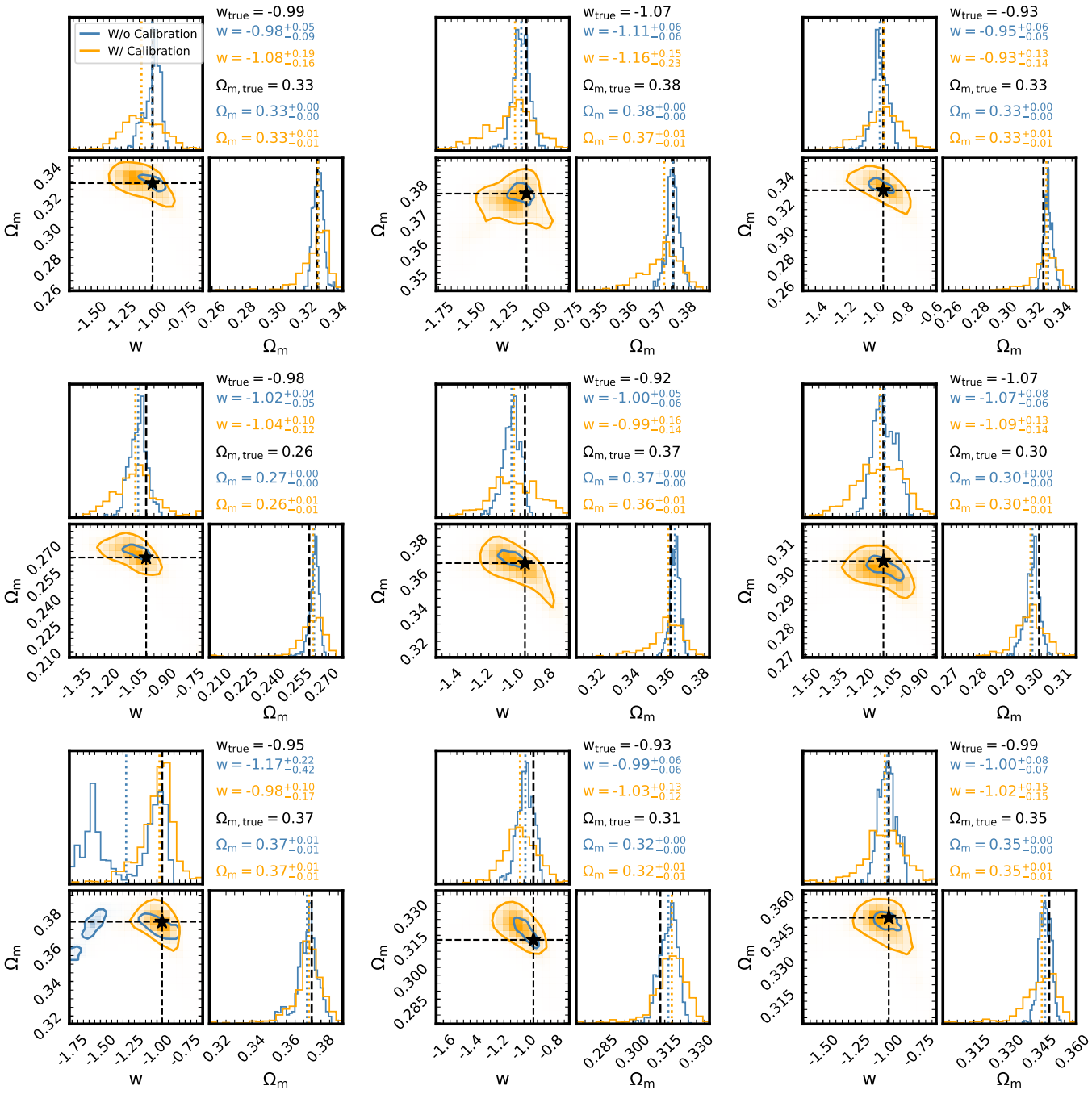

Figure 17. Same as Fig. 7, but for Sub-Region 2.

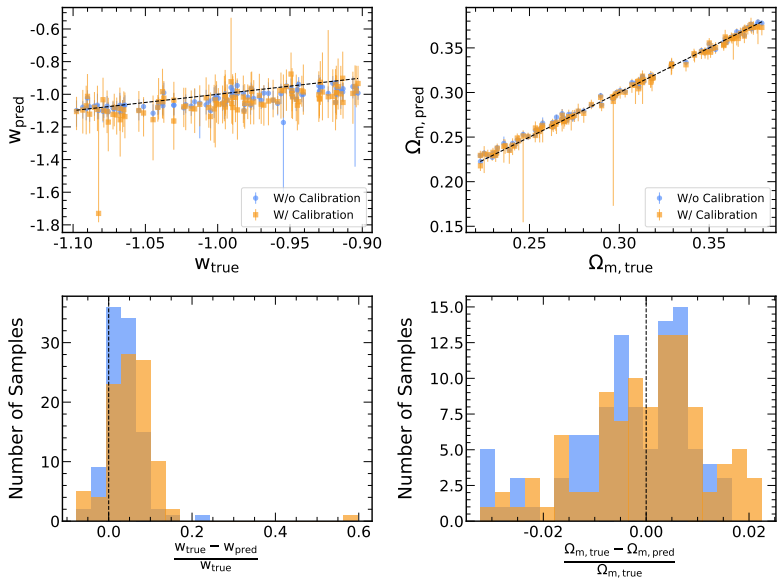

Figure 18. Same as Fig. 8, but for Sub-Region 2.

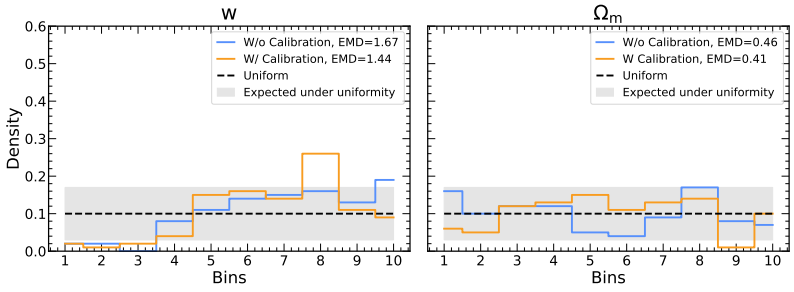

Figure 19. Same as Fig. 9, but for Sub-Region 2.

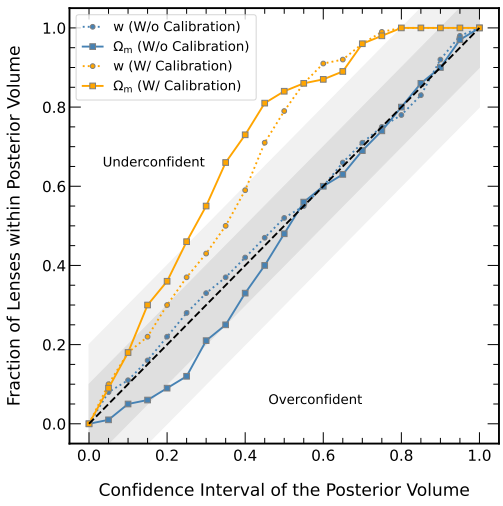

Figure 20. Same as Fig. 10, but for Sub-Region 2.

B.3. *Sub-Region 3*

Posterior Contours (Fig. 21): Without calibration, most contours exclude the true value. With calibration, seven of the nine contours include the true value.

Parity and Residuals (Fig. 22): There is almost no change in bias with calibration: there are fewer outliers for both parameters.

Rank Histogram (Fig. 23): The ranks for w are highly right-skewed without calibration and less skewed with calibration. The ranks for Ω_m are highly left-skewed without calibration and less skewed with calibration. With calibration, the EMD is reduced by almost 50% for both.

Posterior Coverage (Fig. 24): Without calibration, the model is highly overconfident for both parameters. With calibration, the model is nearer to perfect confidence.

For both parameters, the model is biased with and without calibration, but it is nearly perfectly confident with calibration.

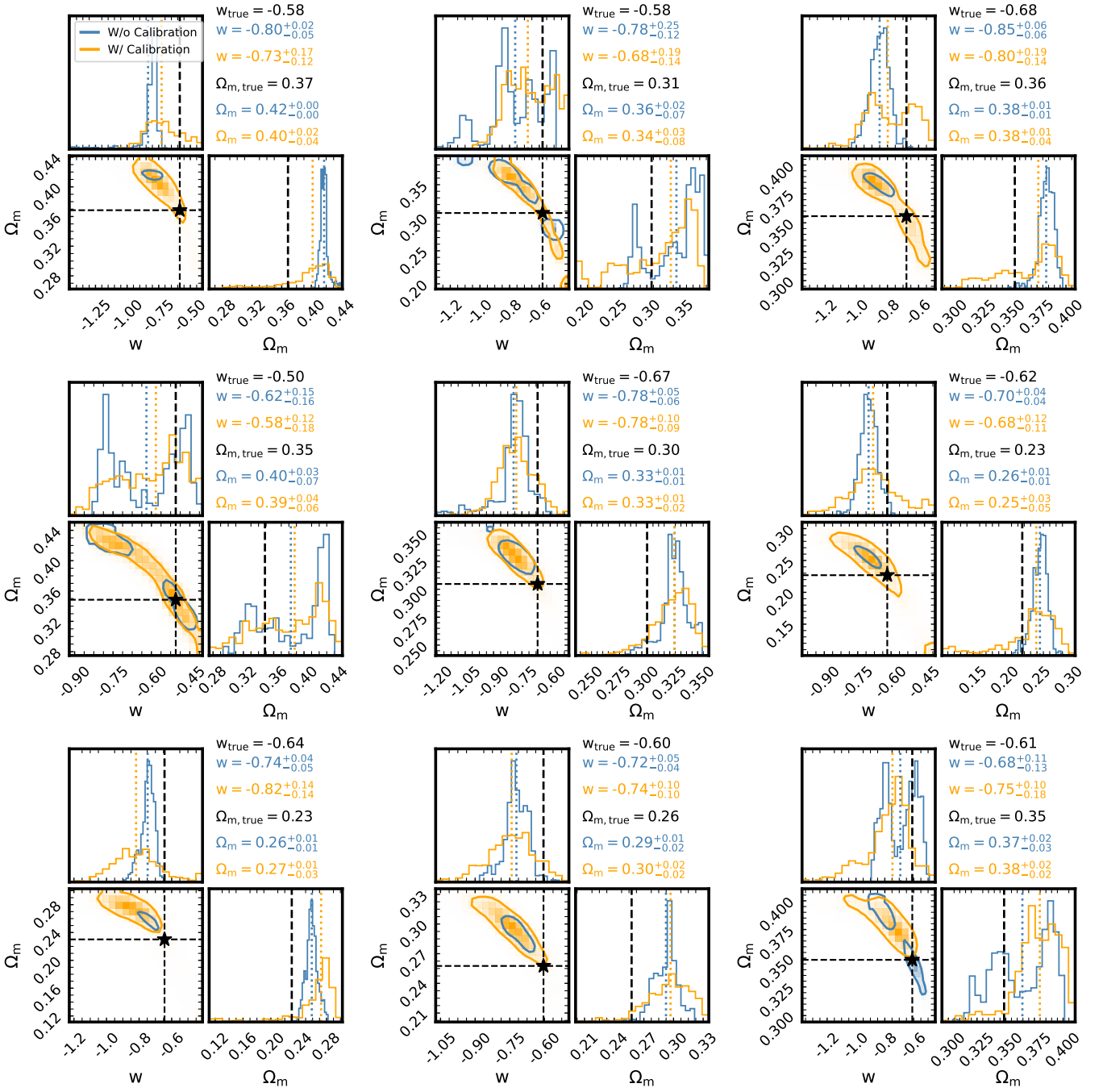

Figure 21. Same as Fig. 7, but for Sub-Region 3.

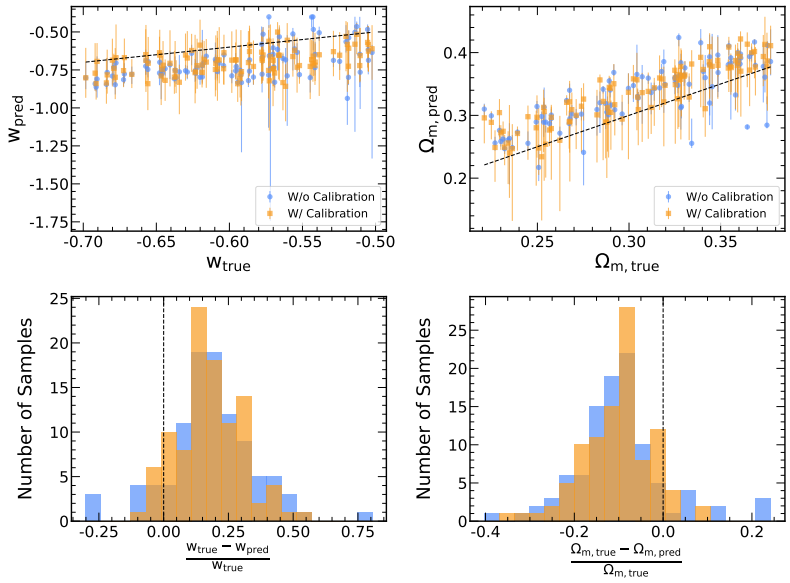

Figure 22. Same as Fig. 8, but for Sub-Region 3.

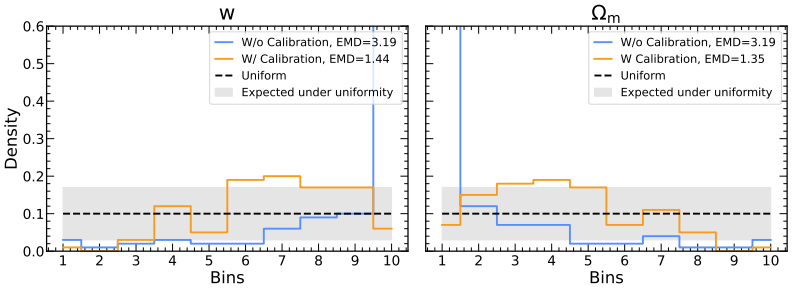

Figure 23. Same as Fig. 9, but for Sub-Region 3.

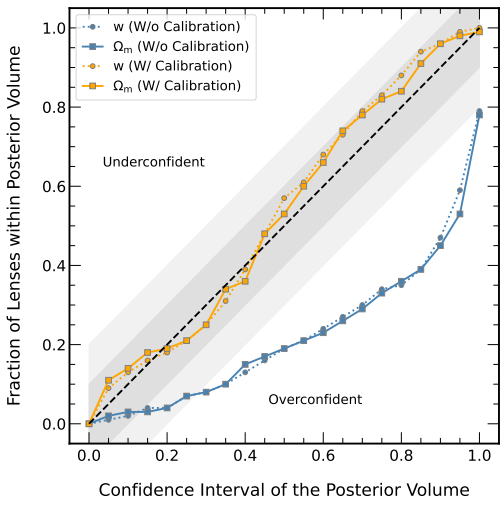

Figure 24. Same as Fig. 10, but for Sub-Region 3.

B.4. *Sub-Region 4*

Posterior Contours (Fig. 25): Contours without calibration include the true value in five out of nine examples. Contours with calibration include the true value in eight of out nine examples. Those models disagree in one example.

Parity and Residuals (Fig. 26): Without calibration, the model is less biased, but has a large number of outliers for both parameters. With calibration, for both parameters, the outliers are lessened significantly, but there is a slight bias.

Rank Histogram (Fig. 27): For both parameters, without calibration, the ranks are nearly uniform. With calibration, there is slight left-skew for both parameters. The EMD is more than doubled with calibration.

Posterior Coverage (Fig. 28): Without calibraiton, the model is slightly overconfident for both parameters. With calibraiton, the model is moderately underconfident.

With calibration, for both parameters, the model is slightly reduced in accuracy, but is made underconfident.

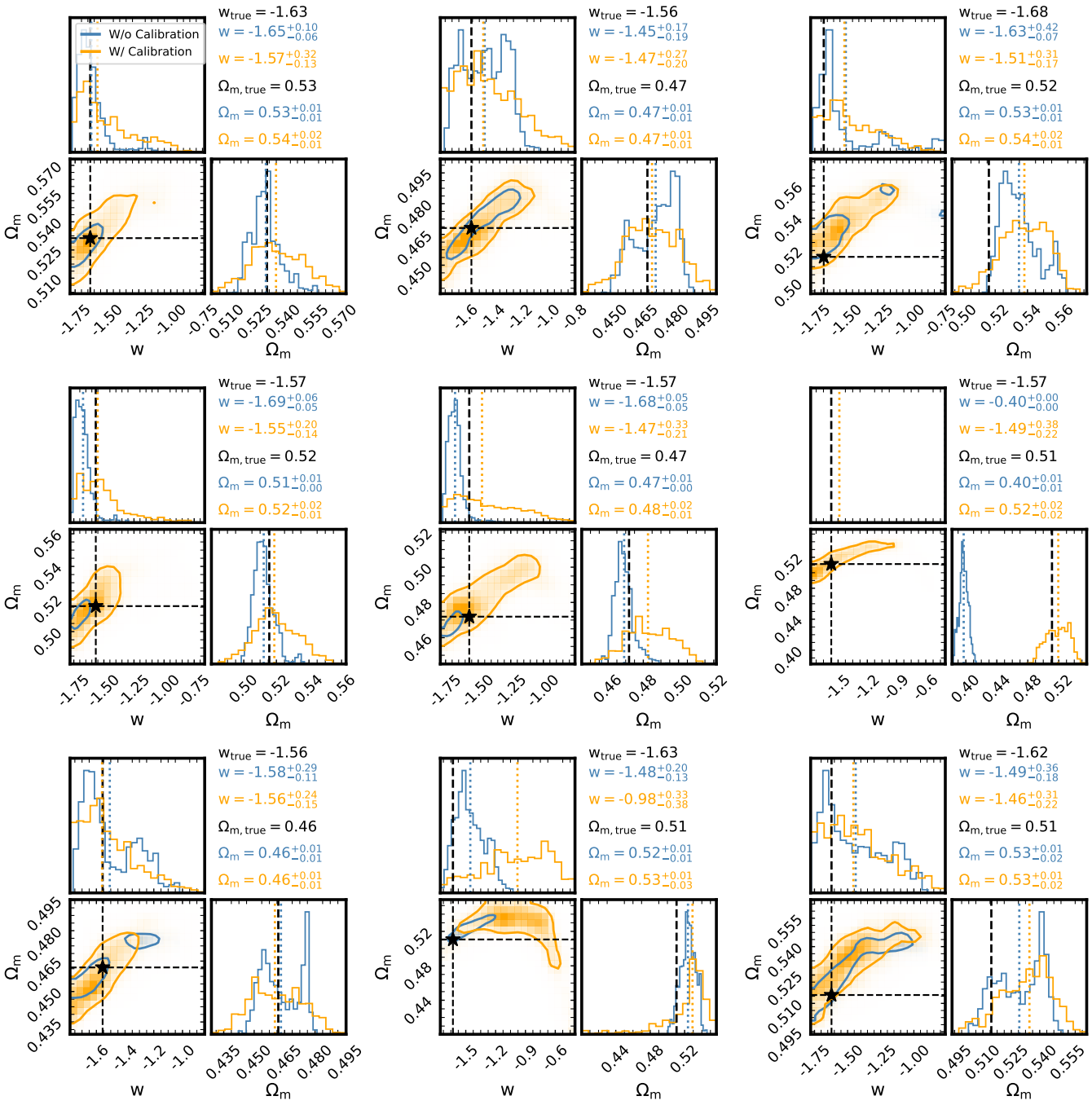

Figure 25. Same as Fig. 7, but for Sub-Region 4.

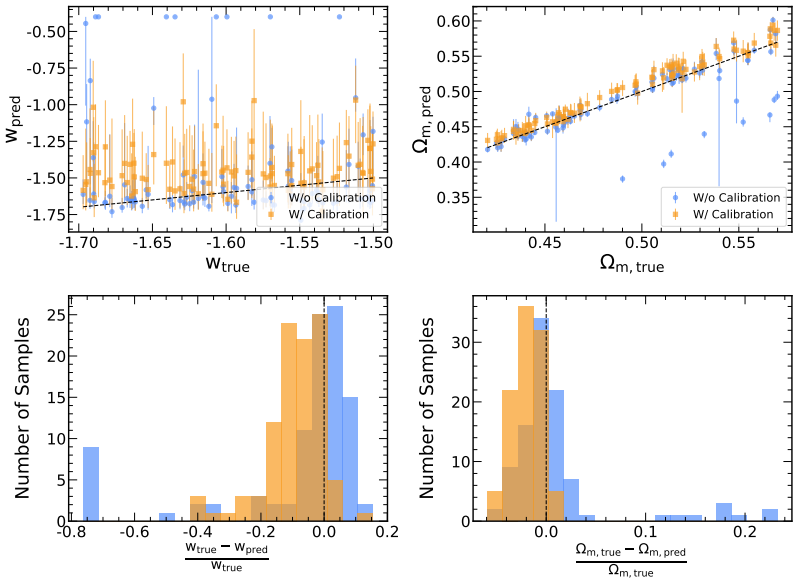

Figure 26. Same as Fig. 8, but for Sub-Region 4.

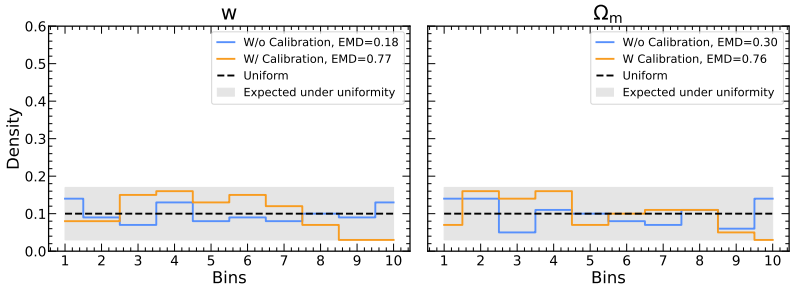

Figure 27. Same as Fig. 9, but for Sub-Region 4.

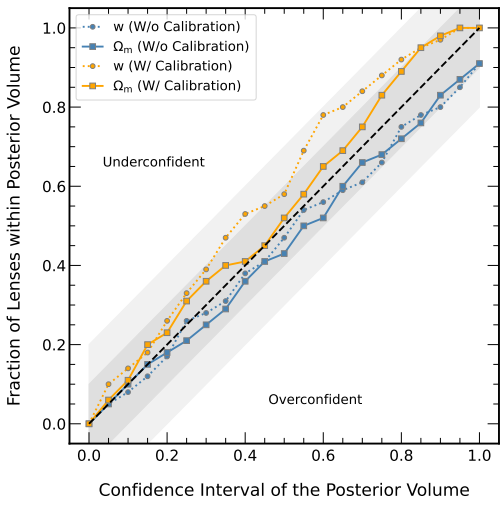

Figure 28. Same as Fig. 10, but for Sub-Region 4.

B.5. *Sub-Region 5*

Posterior Contours (Fig. 29): Without calibration, the contours exclude one true value out of the nine examples. With calibration the contours are larger and don't exclude any true values.

Parity and Residuals (Fig. 30): Without calibration, the model is unbiased for both parameters, but has a large number of outliers. With calibration, the model has no outliers, and it is unibased for w, while having a slight bias for Ω_m.

Rank Histogram (Fig. 31): Without calibration, w ranks are slightly left-skewed, and with calibration, they are $\cap$-shaped. Without calibration, the Ω_m ranks are highly right-skewed, and with calibration, they are $\cap$-shaped and slightly right-skewed. The EMD for w is nearly doubled with calibration, and it is nearly halved for Ω_m.

Posterior Coverage (Fig. 32): Without calibration, the model is moderately undeconfident for w and moderately overconfident for Ω_m. With calibration, the model is highly underconfident for w and partially S-shaped for Ω_m indicating that the posterior is overconfident in the centre and underconfident in the tails.

For both parameters, with calibration, the model's accuracy is mostly unchanged, but it is made underconfident (to different degrees).

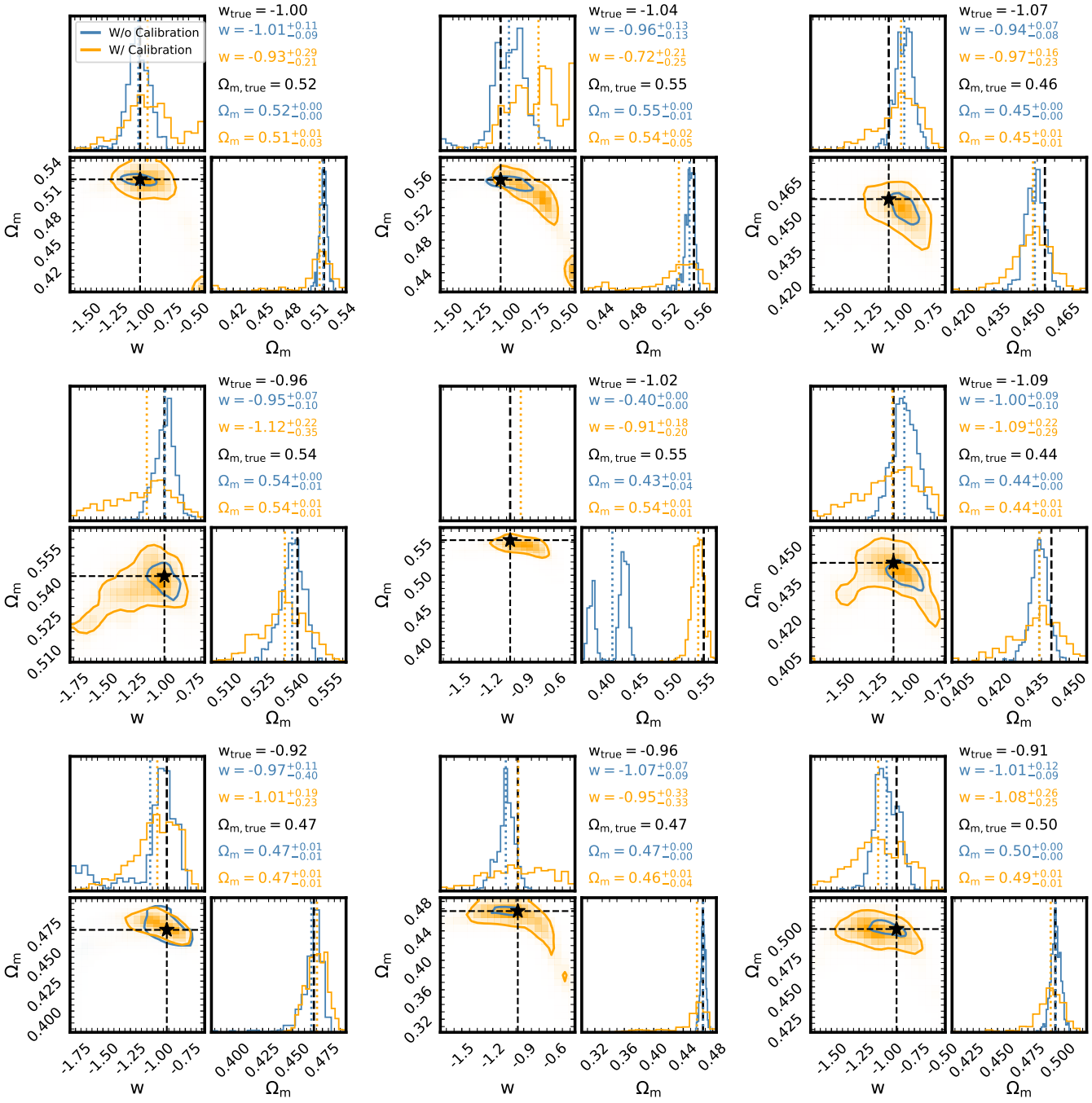

Figure 29. Same as Fig. 7, but for Sub-Region 5.

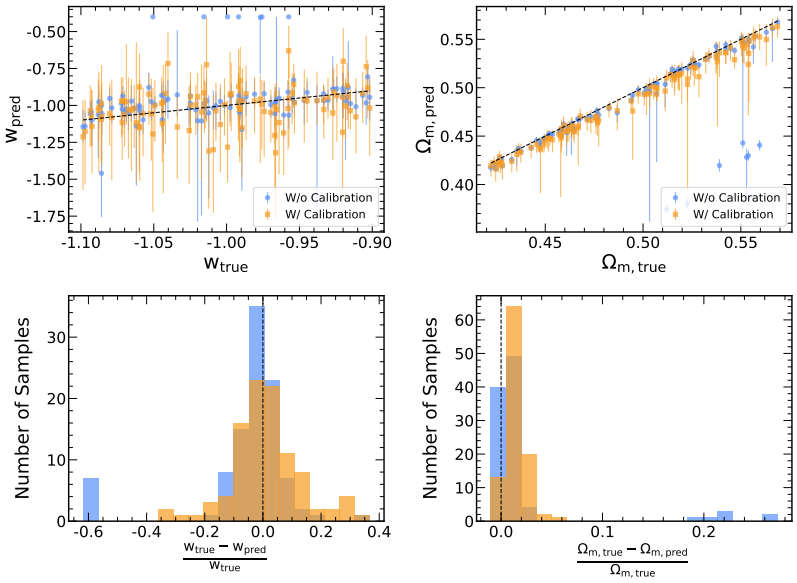

Figure 30. Same as Fig. 8, but for Sub-Region 5.

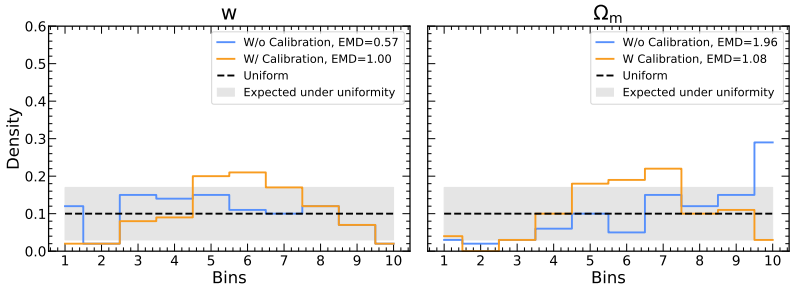

Figure 31. Same as Fig. 9, but for Sub-Region 5.

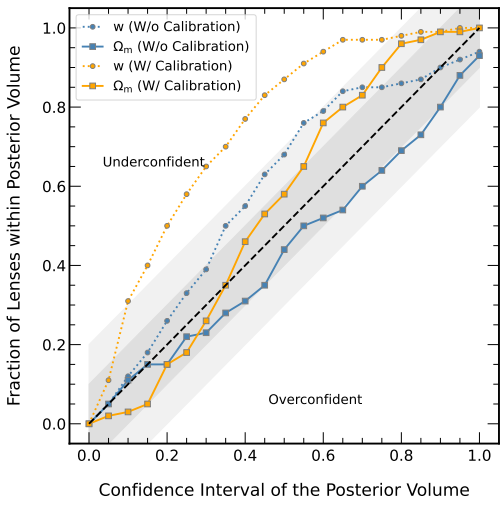

Figure 32. Same as Fig. 10, but for Sub-Region 5.

B.6. *Sub-Region 6*

Posterior Contours (Fig. 33): Without calibration, the model excludes the true value in the majority of examples. With calibration, the model contours are larger and include all true values.

Parity and Residuals (Fig. 34): For both parameters, without calibration, the model has many outliers. For Ω_m, the model is nearly bimodal, and thus highly biased. With calibration, the model remains equivalently biased, but has many fewer outliers.

Rank Histogram (Fig. 35): Without calibration, the ranks are $\cup$-shaped for both parameters. With calibration, the ranks become $\cap$-shaped – but also slightly right-skewed for w and slightly left-skewed for Ω_m. With calibration, the EMD is very slightly reduced for both parameters.

Posterior Coverage (Fig. 36): For both parameters, without calibration, the models are equally and highly overconfident. With calibration, the models are equally and moderately underconfident.

With calibration, the model is mostly unchanged with respect to accuracy, but it is made more conservative in terms of confidence.

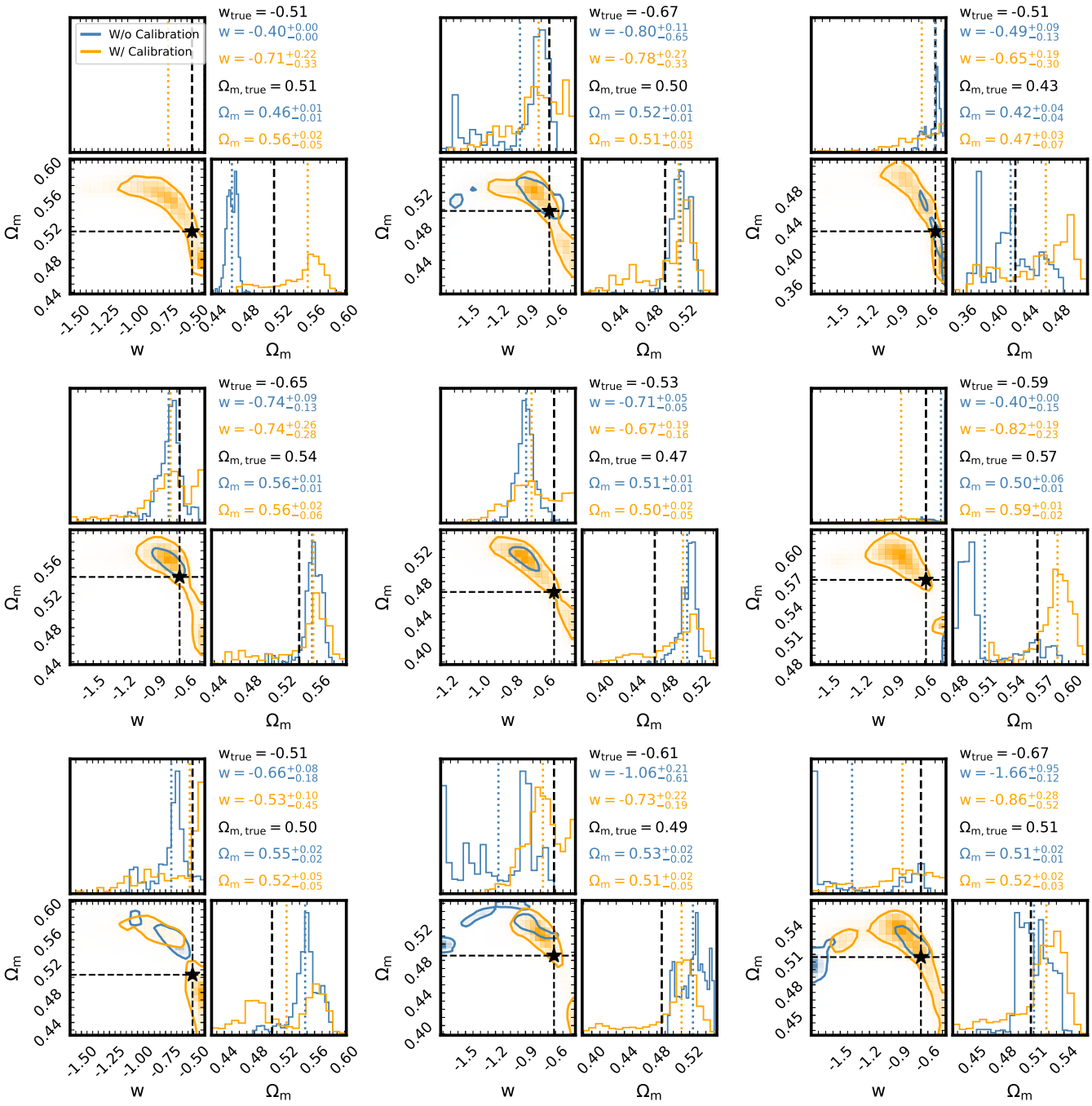

Figure 33. Same as Fig. 7, but for Sub-Region 6.

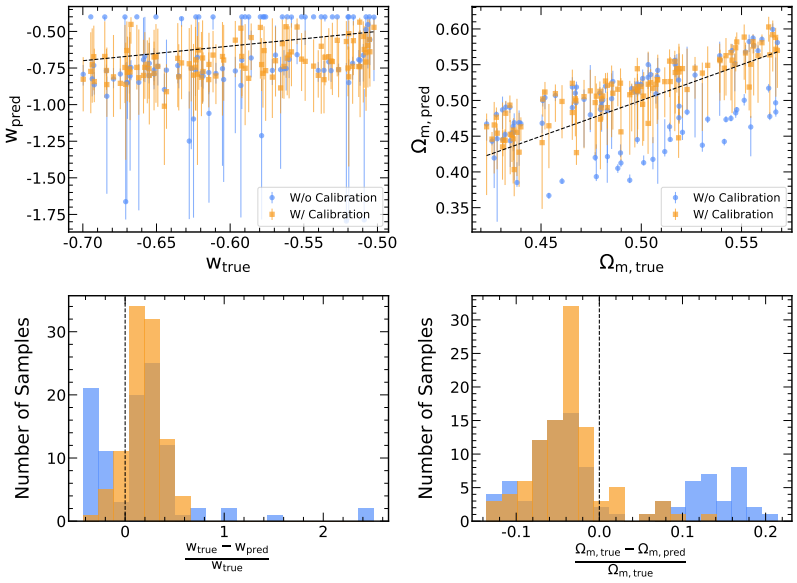

Figure 34. Same as Fig. 8, but for Sub-Region 6.

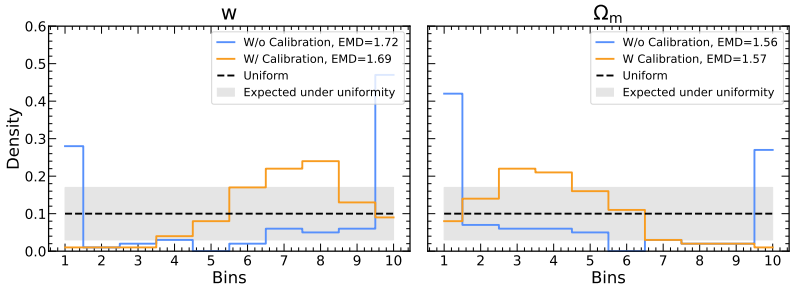

Figure 35. Same as Fig. 9, but for Sub-Region 6.

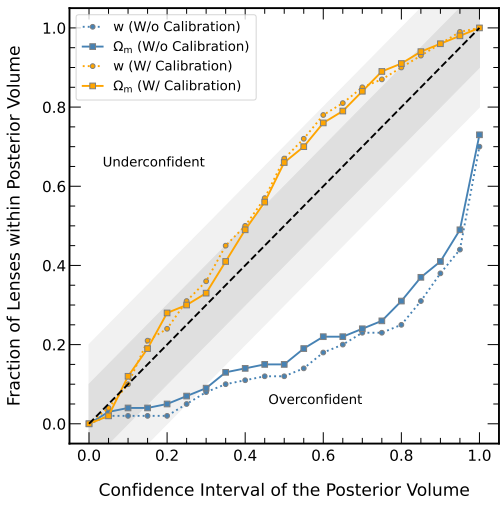

Figure 36. Same as Fig. 10, but for Sub-Region 6.

B.7. *Sub-Region 7*

Posterior Contours (Fig. 37): Without calibration, the model contours exclude true values for almost all the examples, but include true values in all examples with calibration.

Parity and Residuals (Fig. 38): For w, without calibration, the model is unbiased, but has many outliers. For Ω_m, the model is nearly bimodal, and thus highly biased. With calibration, for w, the model is more biased, but with fewer outliers from the main distribution. For Ω_m, the model is less biased.

Rank Histogram (Fig. 39): Without calibration, the ranks are highly left-skewed for w and highly right-skewed for Ω_m. With calibration, the ranks are moderately left-skewed for both parameters. EMD is unchanged for w with calibration and is increased for Ω_m with calibration.

Posterior Coverage (Fig. 40): Without calibration, the models are catastrophically misspecified for both parameters. With calibration, the model is mostly overconfident for w and moderately underconfident for Ω_m.

For both parameters, the model is improved with calibration, but remains overconfident for w.

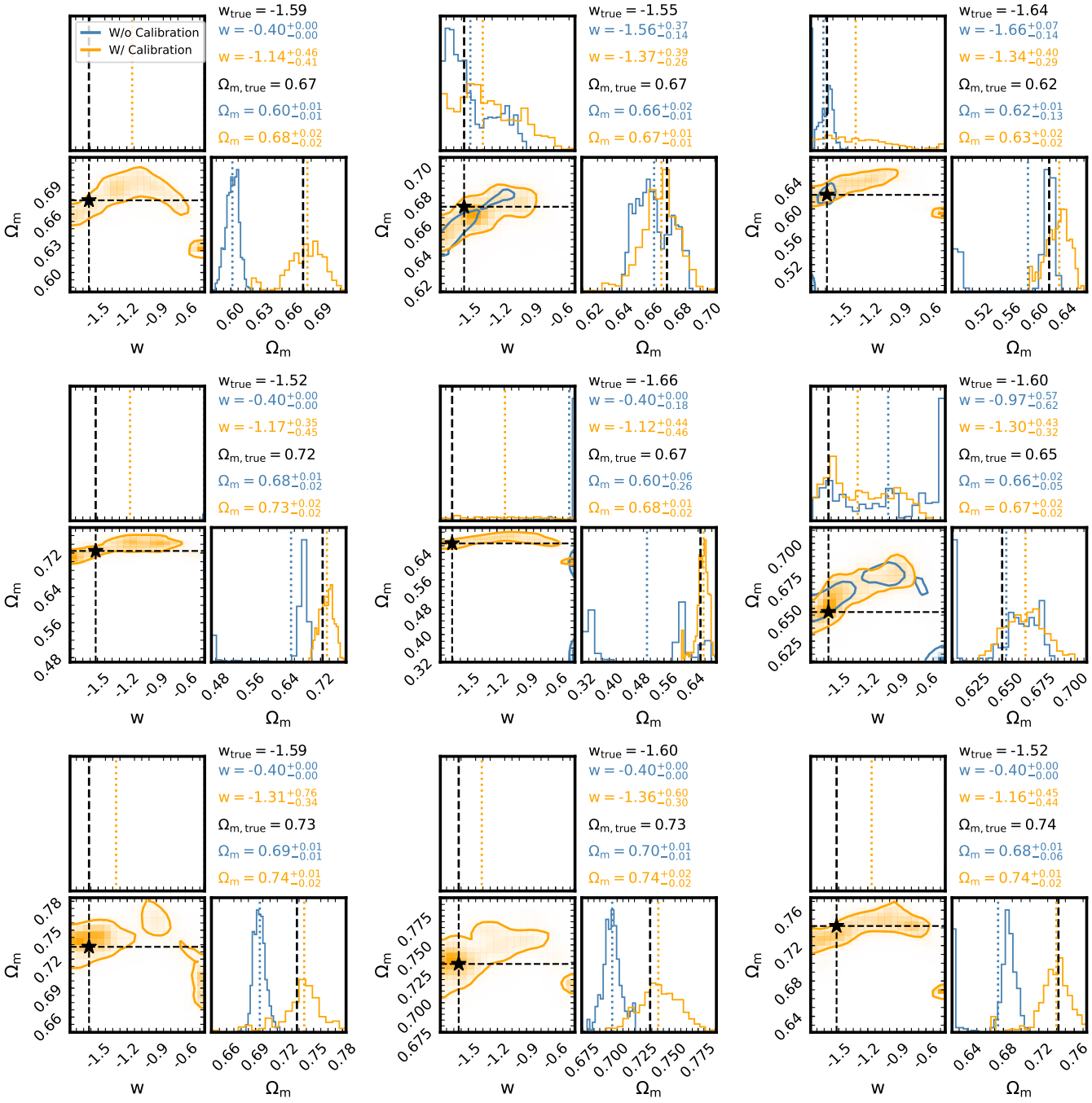

Figure 37. Same as Fig. 7, but for Sub-Region 7.

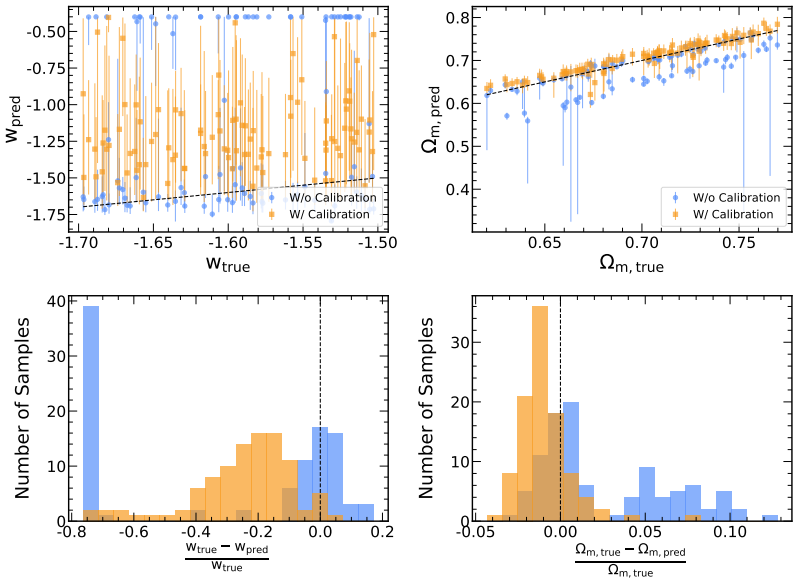

Figure 38. Same as Fig. 8, but for Sub-Region 7.

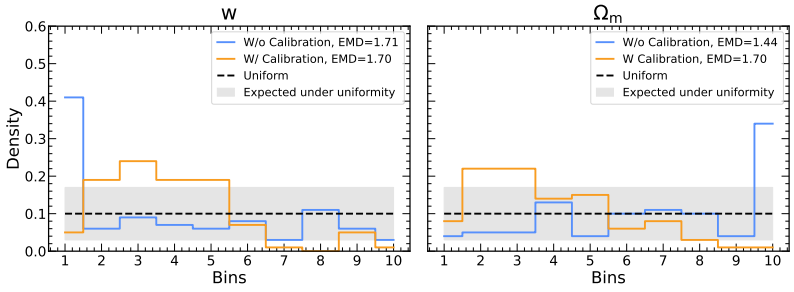

Figure 39. Same as Fig. 9, but for Sub-Region 7.

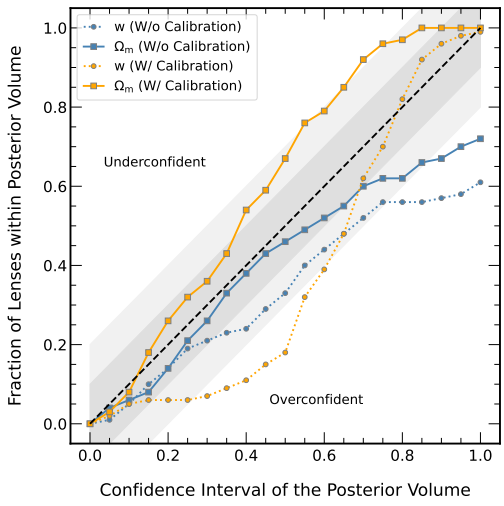

Figure 40. Same as Fig. 10, but for Sub-Region 7.

B.8. *Sub-Region 8*

Posterior Contours (Fig. 41): Without calibration, the model contours exclude the true value for nearly half the examples. With calibration, the model contours exclude true values in two of the examples.

Parity and Residuals (Fig. 42): Without calbiration, the parity is bimodal in both parameters. With calibration, the model parity is unimodal and unbiased for w, and unimodal and slightly biased for Ω_m.

Rank Histogram (Fig. 43): Without calibration, the w ranks are highly left-skewed and the Ω_m ranks are highly right skewed. With calibration, this skewness persists, but is reduced. With calibration, the EMD for w is reduced by over 70%, the EMD for Ω_m is reduced by over 40%.

Posterior Coverage (Fig. 44): Without calibration, the models are catastrophically misspecified for both parameters. With calibration, the model is moderately underconfident for w and mostly overconfident Ω_m – but no long catastrophically misspecified.

Calibration improves the model behavior for both parameters, but remains overconfident for Ω_m.

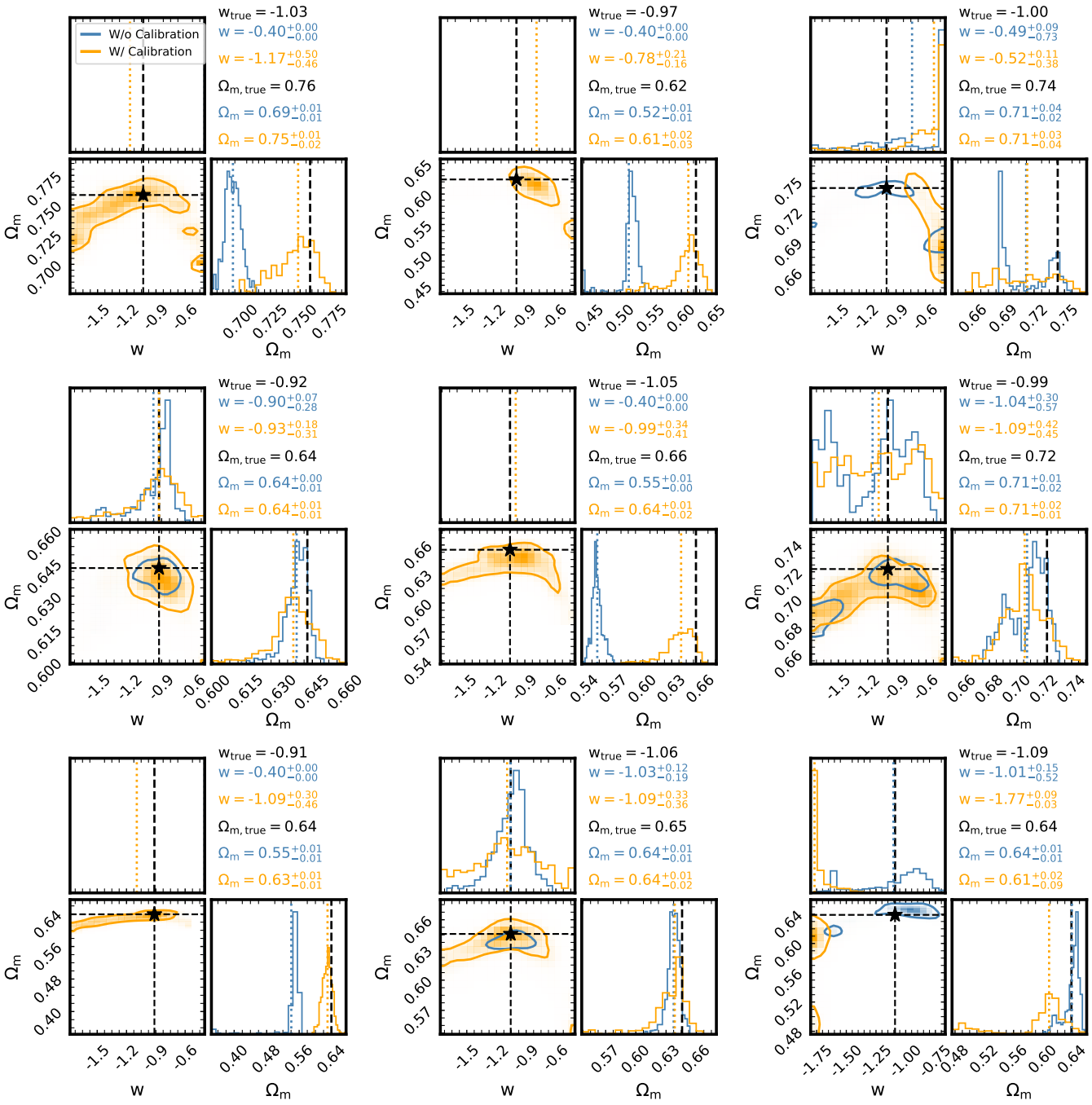

Figure 41. Same as Fig. 7, but for Sub-Region 8.

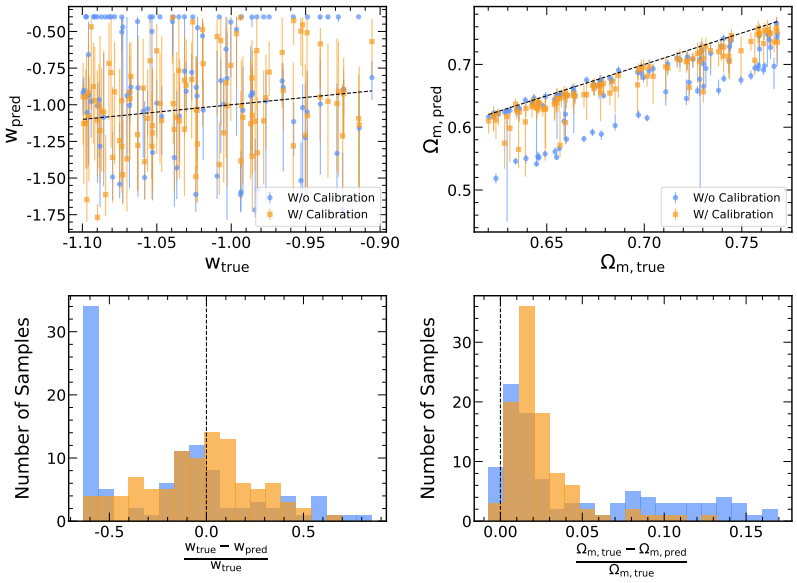

Figure 42. Same as Fig. 8, but for Sub-Region 8.

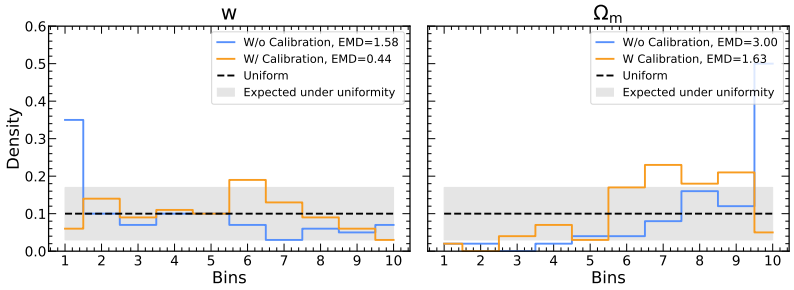

Figure 43. Same as Fig. 9, but for Sub-Region 8.

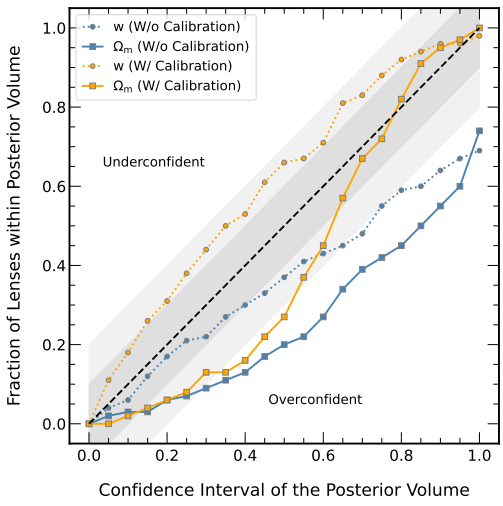

Figure 44. Same as Fig. 10, but for Sub-Region 8.

B.9. *Sub-Region 9*

Posterior Contours (Fig. 45): Without calibration, the model excludes the true value in all nine examples. With calibration, the model includes the true value in all nine examples.

Parity and Residuals (Fig. 46): Without calibration, the model parity is bimodal and has outliers for both parameters. With calibration, the modal nearly unimodal and slightly biased for w and unimodal for Ω_m.

Rank Histogram (Fig. 47): Without calibration, the ranks for w are highly left-skewed, and for Ω_m highly right-skewed. With calibration, the w ranks are moderately right-skewed, and the Ω_m ranks are nearly uniform. With calibration, the EMD is increased significantly for w and decreased by over 50% for Ω_m.

Posterior Coverage (Fig. 48): Without calibration, the model is overconfident and misspecified for both parameters. With calibration, the model is nearly perfectly confident for w and moderately underconfident for Ω_m.

The model is made underconfident and well-specifed with calibration, with slight bias.

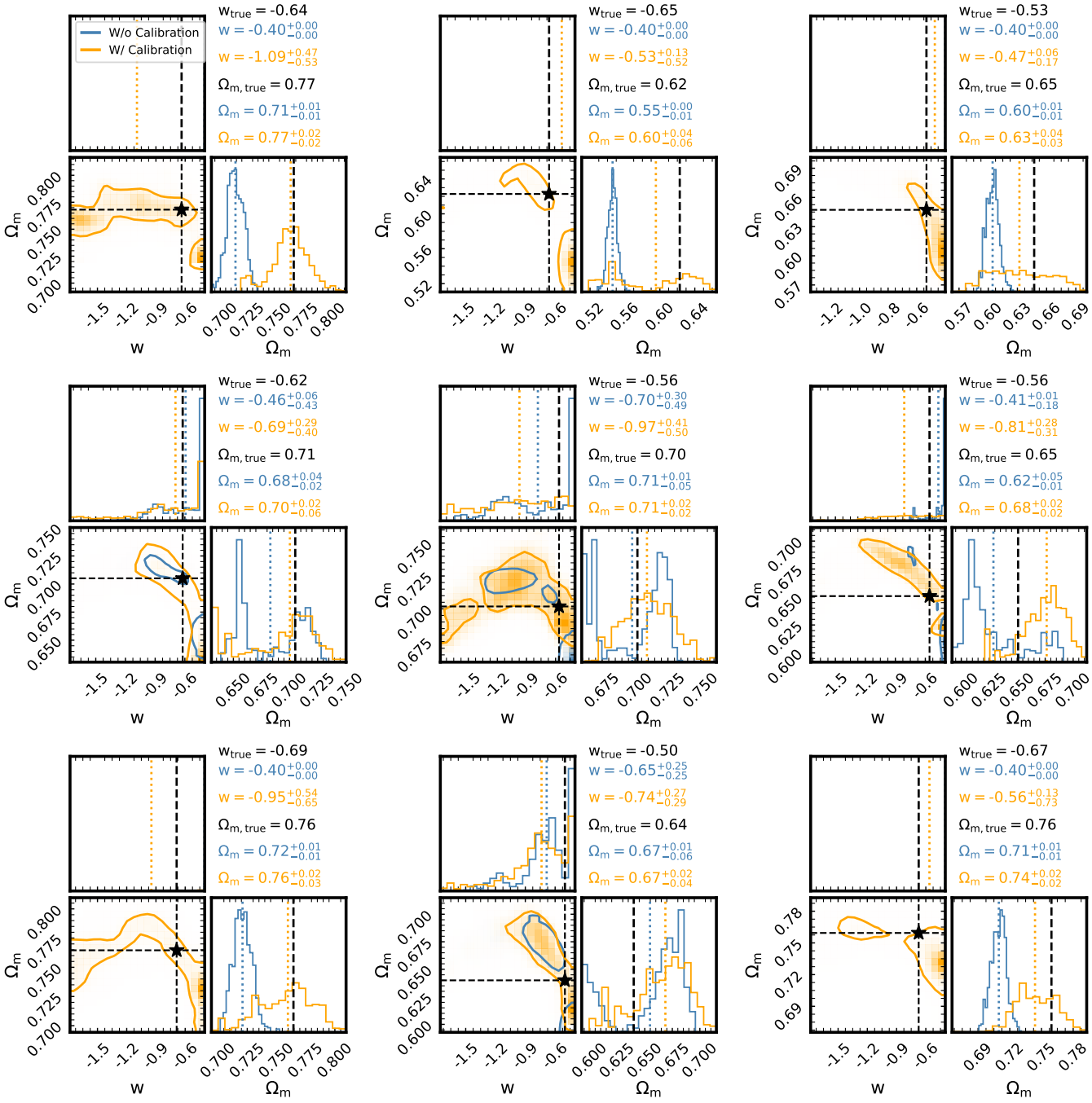

Figure 45. Same as Fig. 7, but for Sub-Region 9.

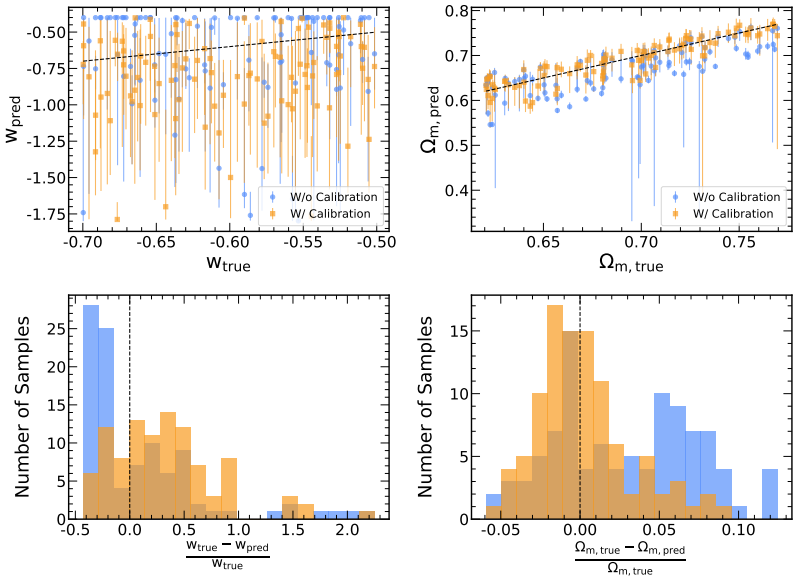

Figure 46. Same as Fig. 8, but for Sub-Region 9.

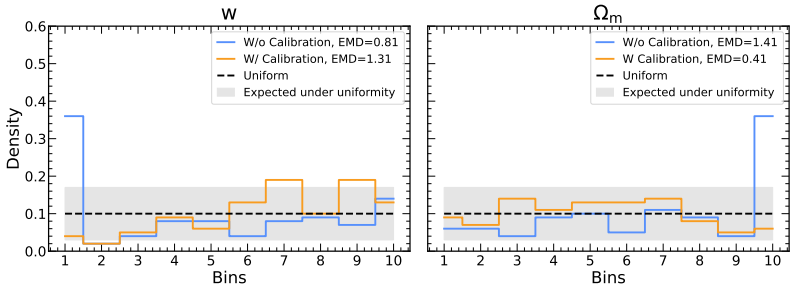

Figure 47. Same as Fig. 9, but for Sub-Region 9.

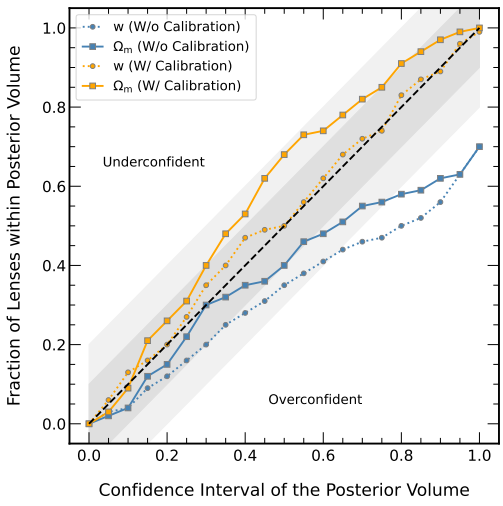

Figure 48. Same as Fig. 10, but for Sub-Region 9.

REFERENCES

Abadi, M., Agarwal, A., Barham, P., et al. 2016, arXiv e-prints, arXiv:1603.04467, doi: 10.48550/arXiv.1603.04467

Anau Montel, N., Alvey, J., & Weniger, C. 2024, Monthly Notices of the Royal Astronomical Society, 530, 4107, doi: 10.1093/mnras/stae1130

Astropy Collaboration, Robitaille, T. P., Tollerud, E. J., et al. 2013, Astronomy & Astrophysics, 558, A33, doi: 10.1051/0004-6361/201322068

Astropy Collaboration, Price-Whelan, A. M., Sipőcz, B. M., et al. 2018, The Astronomical Journal, 156, 123, doi: 10.3847/1538-3881/aabc4f

Avirett-Mackenzie, M. S., & Tojeiro, R. 2021, in American Astronomical Society Meeting Abstracts, Vol. 237, American Astronomical Society Meeting Abstracts #237, 554.04

Barco, G. M., Legin, R., Stone, C., Hezaveh, Y., & Perreault-Levasseur, L. 2025, arXiv e-prints, arXiv:2511.04792, doi: 10.48550/arXiv.2511.04792

Bastide, P., Estoup, A., Marin, J.-M., & Stoehr, J. 2025, arXiv e-prints, arXiv:2507.08734, doi: 10.48550/arXiv.2507.08734

Biesiada, M., Piórkowska, A., & Malec, B. 2010, Monthly Notices of the Royal Astronomical Society, 406, 1055, doi: 10.1111/j.1365-2966.2010.16725.x

Birrer, S., & Amara, A. 2018, Physics of the Dark Universe, 22, 189, doi: 10.1016/j.dark.2018.11.002

Birrer, S., Amara, A., & Refregier, A. 2015, The Astrophysical Journal, 813, 102, doi: 10.1088/0004-637X/813/2/102

Brehmer, J., Louppe, G., Pavez, J., & Cranmer, K. 2020, Proceedings of the National Academy of Sciences, 117, 5242, doi: 10.1073/pnas.1915980117

Brehmer, J., Mishra-Sharma, S., Hermans, J., Louppe, G., & Cranmer, K. 2019, The Astrophysical Journal, 886, 49, doi: 10.3847/1538-4357/ab4c41

Cai, R.-G., & Wang, S.-J. 2026, Research in Astronomy and Astrophysics, 26, 084011, doi: 10.1088/1674-4527/ae842f

Cao, S., Biesiada, M., Gavazzi, R., Piórkowska, A., & Zhu, Z.-H. 2015, The Astrophysical Journal, 806, 185, doi: 10.1088/0004-637X/806/2/185

Cao, X., Li, R., Li, N., et al. 2024, Monthly Notices of the Royal Astronomical Society, 533, 1960, doi: 10.1093/mnras/stae1865

Chen, Y., Li, R., Shu, Y., & Cao, X. 2019, Monthly Notices of the Royal Astronomical Society, 488, 3745, doi: 10.1093/mnras/stz1902

Ciotti, L., & Bertin, G. 1999, Astronomy & Astrophysics, 352, 447, doi: 10.48550/arXiv.astro-ph/9911078

Ćiprijanović, A., Lewis, A., Pedro, K., et al. 2023, Machine Learning: Science and Technology, 4, 025013, doi: 10.1088/2632-2153/acca5f

Cobb, A. D., Matejek, B., Elenius, D., Roy, A., & Jha, S. 2023, arXiv e-prints, arXiv:2311.10571, doi: 10.48550/arXiv.2311.10571

Cole, A., Miller, B. K., Witte, S. J., et al. 2022, Journal of Cosmology and Astroparticle Physics, 2022, 004, doi: 10.1088/1475-7516/2022/09/004

Collett, T. E. 2015, The Astrophysical Journal, 811, 20, doi: 10.1088/0004-637X/811/1/20

Collett, T. E., Sonnenfeld, A., Frohmaier, C., et al. 2023, The Messenger, 190, 49, doi: 10.18727/0722-6691/5313

Cranmer, K., Brehmer, J., & Louppe, G. 2020, Proceedings of the National Academy of Science, 117, 30055, doi: 10.1073/pnas.1912789117

Cranmer, K., Pavez, J., & Louppe, G. 2015, arXiv e-prints, arXiv:1506.02169, doi: 10.48550/arXiv.1506.02169

Dax, M., Green, S. R., Gair, J., et al. 2021, Physical Review Letters, 127, 241103, doi: 10.1103/PhysRevLett.127.241103

Deistler, M., Boelts, J., Steinbach, P., et al. 2025, arXiv e-prints, arXiv:2508.12939, doi: 10.48550/arXiv.2508.12939

Delaunoy, A., Hermans, J., Rozet, F., Wehenkel, A., & Louppe, G. 2022, Advances in Neural Information Processing Systems, 35, 20025, doi: 10.52202/068431-1456

DES Collaboration. 2018, The Astrophysical Journals, 239, 18, doi: 10.3847/1538-4365/aae9f0

Dhanasingham, B., Cyr-Racine, F.-Y., & Gilman, D. 2025, arXiv e-prints, arXiv:2511.17732, doi: 10.48550/arXiv.2511.17732

Di Valentino, E., Mena, O., Pan, S., et al. 2021, Classical and Quantum Gravity, 38, 153001, doi: 10.1088/1361-6382/ac086d

Ding, X., Treu, T., Birrer, S., et al. 2021, Monthly Notices of the Royal Astronomical Society, 503, 1096, doi: 10.1093/mnras/stab484

Dirmeier, S., Albert, C., & Perez-Cruz, F. 2023, arXiv e-prints, arXiv:2308.01054, doi: 10.48550/arXiv.2308.01054

Emma, M., & Ashton, G. 2026, Physical Review D, 113, 124064, doi: 10.1103/f5df-cxyg

Erickson, S., Wagner-Carena, S., Marshall, P., et al. 2025, The Astronomical Journal, 170, 44, doi: 10.3847/1538-3881/add99f

Euclid Collaboration. 2022, Astronomy & Astrophysics, 662, A112, doi: 10.1051/0004-6361/202141938

Fan, Y., & White, S. R. 2025, arXiv e-prints, arXiv:2506.04558, doi: 10.48550/arXiv.2506.04558
Feeney, S. M., Mortlock, D. J., & Dalmasso, N. 2018, Monthly Notices of the Royal Astronomical Society, 476, 3861, doi: 10.1093/mnras/sty418
Ferrami, G., & Wyithe, J. S. B. 2025, Monthly Notices of the Royal Astronomical Society, 537, 779, doi: 10.1093/mnras/staf089
Foreman-Mackey, D., Hogg, D. W., Lang, D., & Goodman, J. 2013, Publications of the Astronomical Society of the Pacific, 125, 306, doi: 10.1086/670067
Franco Abellán, G., Anau Montel, N., Savchenko, O., & Weniger, C. 2025, Physical Review D, 112, 103526, doi: 10.1103/ws4b-7qrw
Frazier, D. T., Kelly, R., Drovandi, C., & Warne, D. J. 2024, arXiv e-prints, arXiv:2411.12068, doi: 10.48550/arXiv.2411.12068
Freedman, W. L. 2021, The Astrophysical Journal, 919, 16, doi: 10.3847/1538-4357/ac0e95
Futamase, T., & Yoshida, S. 2001, Progress of Theoretical Physics, 105, 887, doi: 10.1143/PTP.105.887
Gandrakota, A., Zhang, L. H., Puli, A., et al. 2024, Machine Learning: Science and Technology, 5, 035082, doi: 10.1088/2632-2153/ad780c
Givens, C. R., & Shortt, R. M. 1984, Michigan Mathematical Journal, 31, 231. https://api.semanticscholar.org/CorpusID:121338763
Gloeckler, M., Deistler, M., Weilbach, C., Wood, F., & Macke, J. H. 2024, arXiv e-prints, arXiv:2404.09636, doi: 10.48550/arXiv.2404.09636
Green, S. R., Simpson, C., & Gair, J. 2020, Physical Review D, 102, 104057, doi: 10.1103/PhysRevD.102.104057
Greenberg, D. S., Nonnenmacher, M., & Macke, J. H. 2019, in International Conference on Machine Learning. https://api.semanticscholar.org/CorpusID:159041084
Hastings, W. K. 1970, Biometrika, 57, 97, doi: 10.1093/biomet/57.1.97
He, K., Zhang, X., Ren, S., & Sun, J. 2015, arXiv e-prints, arXiv:1512.03385, doi: 10.48550/arXiv.1512.03385
Hermans, J., Begy, V., & Louppe, G. 2020, in International Conference on Machine Learning, PMLR, 4239–4248, doi: 10.48550/arXiv.1903.04057
Hermans, J., Delaunoy, A., Rozet, F., et al. 2021, arXiv e-prints, arXiv:2110.06581, doi: 10.48550/arXiv.2110.06581
Hezaveh, Y. D., Perreault Levasseur, L., & Marshall, P. J. 2017, Nature, 548, 555, doi: 10.1038/nature23463
Holloway, P., Verma, A., Marshall, P. J., More, A., & Tecza, M. 2023, Monthly Notices of the Royal Astronomical Society, 525, 2341, doi: 10.1093/mnras/stad2371
Huterer, D. 2023, The European Physical Journal Plus, 138, 1
Ivezic, Z., Axelrod, T., Brandt, W. N., et al. 2008, Serbian Astronomical Journal, 176, 1, doi: 10.2298/SAJ0876001I
Joseph, M., Aloni, D., Schmaltz, M., Sivarajan, E. N., & Weiner, N. 2023, Physical Review D, 108, 023520, doi: 10.1103/PhysRevD.108.023520
Kamionkowski, M., & Riess, A. G. 2023, Annual Review of Nuclear and Particle Science, 73, 153, doi: 10.1146/annurev-nucl-111422-024107
Khalife, A. R., Zanjani, M. B., Galli, S., et al. 2024, Journal of Cosmology and Astroparticle Physics, 2024, 059, doi: 10.1088/1475-7516/2024/04/059
Kingma, D. P., Salimans, T., Jozefowicz, R., et al. 2016, Advances in Neural Information Processing Systems, 29, doi: 10.48550/arXiv.1606.04934
Kolmus, A., Janquart, J., Baka, T., et al. 2024, arXiv e-prints, arXiv:2403.02443, doi: 10.48550/arXiv.2403.02443
Koopmans, L. V. E. 2006, in EAS Publications Series, Vol. 20, EAS Publications Series, ed. G. A. Mamon, F. Combes, C. Deffayet, & B. Fort (EDP), 161–166, doi: 10.1051/eas:2006064
Kormann, R., Schneider, P., & Bartelmann, M. 1994, Astronomy & Astrophysics, 284, 285
Legin, R., Hezaveh, Y., Perreault Levasseur, L., & Wandelt, B. 2021, in Machine Learning and the Physical Sciences Workshop, 95, doi: 10.48550/arXiv.2112.05278
Legin, R., Hezaveh, Y., Perreault-Levasseur, L., & Wandelt, B. 2023, The Astrophysical Journal, 943, 4, doi: 10.3847/1538-4357/aca7c2
Leizerovich, M., Landau, S. J., & Scóccola, C. G. 2023, arXiv e-prints, arXiv:2312.08542, doi: 10.48550/arXiv.2312.08542
Lemos, P., Coogan, A., Hezaveh, Y., & Perreault-Levasseur, L. 2023, 40th International Conference on Machine Learning, 202, 19256, doi: 10.48550/arXiv.2302.03026
Leyde, K., Green, S. R., Toubiana, A., & Gair, J. 2024, Physical Review D, 109, 064056, doi: 10.1103/PhysRevD.109.064056
Li, H., & Chen, Y. 2023, Physics of the Dark Universe, 41, 101234, doi: 10.1016/j.dark.2023.101234
Li, T., Collett, T. E., Krawczyk, C. M., & Enzi, W. 2024, Monthly Notices of the Royal Astronomical Society, 527, 5311, doi: 10.1093/mnras/stad3514
Li, X., Keeley, R. E., Shafieloo, A., & Liao, K. 2024, The Astrophysical Journal, 960, 103, doi: 10.3847/1538-4357/ad0f19
Lines, N. E. P., Li, T., Collett, T. E., et al. 2025, Nature Astronomy, 9, 1116, doi: 10.1038/s41550-025-02616-5

Linhart, J., Cardoso, G. V., Gramfort, A., Corff, S. L., & Rodrigues, P. L. 2024, arXiv preprint arXiv:2404.07593, doi: 10.48550/arXiv.2404.07593

Lueckmann, J.-M., Boelts, J., Greenberg, D., Goncalves, P., & Macke, J. 2021, in International Conference on Artificial Intelligence and Statistics, PMLR, 343–351, doi: 10.48550/arXiv.2101.04653

McCarthy, I. G., Salcido, J., Schaye, J., et al. 2023, Monthly Notices of the Royal Astronomical Society, 526, 5494, doi: 10.1093/mnras/stad3107

Miller, B., Cole, A., Forré, P., Louppe, G., & Weniger, C. 2021, Advances in Neural Information Processing Systems, 34, 129, doi: 10.48550/arXiv.2107.01214

Miller, B. K., Weniger, C., & Forré, P. 2022, Advances in Neural Information Processing Systems, 35, 3262, doi: 10.52202/068431-0236

Morgan, R., Nord, B., Birrer, S., Lin, J., & Poh, J. 2021, The Journal of Open Source Software, 6, 2854, doi: 10.21105/joss.02854

Oguri, M., & Marshall, P. J. 2010, Monthly Notices of the Royal Astronomical Society, 405, 2579, doi: 10.1111/j.1365-2966.2010.16639.x

Pandya, S., Patel, P., Nord, B. D., Walmsley, M., & Ćiprijanović, A. 2025, Machine Learning: Science and Technology, 6, 035032, doi: 10.1088/2632-2153/adf701

Pantos, I., & Perivolaropoulos, L. 2026, Physics of the Dark Universe, 52, 102286, doi: 10.1016/j.dark.2026.102286

Papamakarios, G., & Murray, I. 2016, arXiv: Machine Learning. https://api.semanticscholar.org/CorpusID:8401036

Papamakarios, G., Pavlakou, T., & Murray, I. 2017, Advances in Neural Information Processing Systems, 30, doi: 10.48550/arXiv.1705.07057

Papamakarios, G., Sterratt, D., & Murray, I. 2019, in The 22nd international conference on artificial intelligence and statistics, PMLR, 837–848, doi: 10.48550/arXiv.1805.07226

Planck Collaboration. 2020, Astronomy & Astrophysics, 641, A6, doi: 10.1051/0004-6361/201833910

Poh, J., Samudre, A., Ćiprijanović, A., et al. 2025, Journal of Cosmology and Astroparticle Physics, 2025, 053, doi: 10.1088/1475-7516/2025/05/053

Poulin, V., Bernal, J. L., Kovetz, E. D., & Kamionkowski, M. 2023, Physical Review D, 107, 123538, doi: 10.1103/PhysRevD.107.123538

Puli, A., Zhang, L. H., Oermann, E. K., & Ranganath, R. 2021, arXiv e-prints, arXiv:2107.00520, doi: 10.48550/arXiv.2107.00520

Refsdal, S. 1964, Monthly Notices of the Royal Astronomical Society, 128, 307, doi: 10.1093/mnras/128.4.307

Remy, B., Lanusse, F., Jeffrey, N., et al. 2023, Astronomy & Astrophysics, 672, A51, doi: 10.1051/0004-6361/202243054

Riess, A. G., Yuan, W., Macri, L. M., et al. 2022, The Astrophysical Journall, 934, L7, doi: 10.3847/2041-8213/ac5c5b

Rizvi, S., Pettee, M., & Nachman, B. 2024, Journal of High Energy Physics, 2024, 136, doi: 10.1007/JHEP02(2024)136

Rodrigues, P. L. C., Moreau, T., Louppe, G., & Gramfort, A. 2021, in Proceedings of the 35th International Conference on Neural Information Processing Systems, NIPS '21 (Red Hook, NY, USA: Curran Associates Inc.)

Rosso, H., & Mayo, T. 2025, arXiv preprint arXiv:2512.23748, doi: 10.48550/arXiv.2512.23748

Saha, P., Sluse, D., Wagner, J., & Williams, L. L. R. 2024, Space Science Reviews, 220, 12, doi: 10.1007/s11214-024-01041-w

Sersic, J. L. 1968, Atlas de Galaxias Australes (Observatorio Astronòmico)

Shajib, A. J., Vernardos, G., Collett, T. E., et al. 2024, Space Science Reviews, 220, 87, doi: 10.1007/s11214-024-01105-x

Shajib, A. J., Smith, G. P., Birrer, S., et al. 2025, Philosophical Transactions of the Royal Society of London Series A, 383, 20240117, doi: 10.1098/rsta.2024.0117

Sharrock, L., Simons, J., Liu, S., & Beaumont, M. 2022, arXiv e-prints, arXiv:2210.04872, doi: 10.48550/arXiv.2210.04872

Sonnenfeld, A. 2021, Astronomy & Astrophysics, 656, A153, doi: 10.1051/0004-6361/202142062

Spergel, D., Gehrels, N., Baltay, C., et al. 2015, arXiv e-prints, arXiv:1503.03757, doi: 10.48550/arXiv.1503.03757

Suyu, S. H., Bonvin, V., Courbin, F., et al. 2017, Monthly Notices of the Royal Astronomical Society, 468, 2590, doi: 10.1093/mnras/stx483

Swierc, P., Tamargo-Arizmendi, M., Ćiprijanović, A., & Nord, B. D. 2024, arXiv e-prints, arXiv:2410.16347, doi: 10.48550/arXiv.2410.16347

Talts, S., Betancourt, M., Simpson, D., Vehtari, A., & Gelman, A. 2018, arXiv e-prints, arXiv:1804.06788, doi: 10.48550/arXiv.1804.06788

Tejero-Cantero, A., Boelts, J., Deistler, M., et al. 2020, The Journal of Open Source Software, 5, 2505, doi: 10.21105/joss.02505

Tortora, C., Piedipalumbo, E., & Cardone, V. F. 2004, Monthly Notices of the Royal Astronomical Society, 354, 343, doi: 10.1111/j.1365-2966.2004.08160.x

Tran, D., Ranganath, R., & Blei, D. 2017, Advances in Neural Information Processing Systems, 30

Treu, T. 2010, Annual Review of Astronomy and Astrophysics, 48, 87, doi: 10.1146/annurev-astro-081309-130924

Treu, T., & Shajib, A. J. 2024, in The Hubble constant tension (Springer), 251–276, doi: 10.1007/978-981-99-0177-7_14

Treu, T., Suyu, S. H., & Marshall, P. J. 2022, The Astronomy and Astrophysics Review, 30, 8, doi: 10.1007/s00159-022-00145-y

Treyer, M., Ait-Ouahmed, R., Arnouts, S., et al. 2026, Astronomy & Astrophysics, 707, A105, doi: 10.1051/0004-6361/202557504

Wong, K. C., Suyu, S. H., Chen, G. C.-F., et al. 2020, Monthly Notices of the Royal Astronomical Society, 498, 1420, doi: 10.1093/mnras/stz3094

Zeghal, J., Lanusse, F., Boucaud, A., Remy, B., & Aubourg, E. 2022, in Machine Learning for Astrophysics, 52, doi: 10.48550/arXiv.2207.05636

Zhang, G., Mishra-Sharma, S., & Dvorkin, C. 2022, Monthly Notices of the Royal Astronomical Society, 517, 4317, doi: 10.1093/mnras/stac3014

Zu, L., Giarè, W., Zhang, C., et al. 2026, Nature Astronomy, 10, 457, doi: 10.1038/s41550-025-02733-1